Direct numerical simulation of the flow around a wall-mounted square cylinder under various inflow conditions

Ricardo Vinuesa[a]*, Philipp Schlatter[a], Johan Malm[a], Catherine Mavriplis[b] and Dan S. Henningson[a]

[a]Linné FLOW Centre, KTH Mechanics, Stockholm, Sweden; [b]Deptartment of Mechanical Engineering, University of Ottawa, Ottawa, Canada

The flow around a wall-mounted square cylinder of side d is investigated by means of direct numerical simulation (DNS). The effect of inflow conditions is assessed by considering two different cases with matching momentum-thickness Reynolds numbers $Re_\theta \simeq 1000$ at the obstacle: the first case is a fullyturbulent zero pressure gradient boundary layer, and the second one is a laminar boundary layer with prescribed Blasius inflow profile further upstream. An auxiliary simulation carried out with the pseudo-spectral Fourier–Chebyshev code SIMSON is used to obtain the turbulent time-dependent inflow conditions which are then fed into the main simulation where the actual flow around the cylinder is computed. This main simulation is performed, for both laminar and turbulent-inflows, with the spectral-element method code Nek5000. In both cases the wake is completely turbulent, and we find the same Strouhal number $St \simeq 0.1$, although the two wakes exhibit structural differences for $x > 3d$ downstream of the cylinder. Transition to turbulence is observed in the laminar-inflow case, induced by the recirculation bubble produced upstream of the obstacle, and in the turbulent-inflow simulation the streamwise fluctuations modulate the horseshoe vortex. The wake obtained in our laminar-inflow case is in closer agreement with reference particle image velocimetry measurements of the same geometry, revealing that the experimental boundary layer was not fully turbulent in that dataset, and highlighting the usefulness of DNS to assess the quality of experimental inflow conditions.

Keywords: wall turbulence; direct numerical simulation; three-dimensional flows; separated flows; square-cylinder flow

1. Introduction

The flow around two-dimensional cylinders of different cross-sectional areas has been extensively studied (see for instance the work by Oertel [1] or Zdravkovich [2]) in order to properly characterise turbulent features in a von Kármán vortex street, since it exhibits a more organised flow structure than the one found in a wall-mounted cylinder of finite length. However, the more complex flow encountered in wall-mounted cylinders is characteristic of a number of technological applications of great importance, including calculation of aerodynamic forces on cooling towers, pollutant dispersion in urban environments, impact on pedestrian comfort affected by the streams associated with microclimates of large buildings and structures, heat transfer in electronic boards, vortex generators in aerospace structures or blades in compressors and turbines. It is also crucial to be able to accurately determine

---

*Corresponding author. Email: rvinuesa@mech.kth.se

vortex shedding frequencies in complex geometries for adequate structural design in order to avoid large vibrations induced by resonance. For instance, the flow around one building under the influence of various surface layer conditions was studied experimentally by Corke et al.,[3] and pollutant dispersion in a number of urban environments was characterised by Nagib and Corke [4] and Monnier et al. [5] by means of wind tunnel testing. The relation between surface mounted cylinders and jets emanating from the surface has been studied and characterised by Fric and Roshko.[6]

The development of progressively faster and larger supercomputing centres, combined with the development of more flexible numerical codes, is starting to allow computations of more complex geometries, where the effect of certain idealisations in the computational domain on the flow can now be assessed. For instance, spatially developing boundary layers can be computed now,[7,8] as opposed to the traditional streamwise-periodic flows, and the differences between considering turbulent rectangular duct flows instead of spanwise-periodic channels have recently been discussed.[9]

Aligned with the need to perform numerical simulations of flows closer to industrial applications, the CFD (Computational Fluid Dynamics) Society of Canada organised a Challenge in 2012 aimed at the comparison of a number of computational studies of the flow around a square-section cylinder mounted vertically on a flat plate, using as a benchmark a wind tunnel experiment of the same geometry placed in a zero pressure gradient (ZPG) turbulent boundary layer (TBL). The CFDSC 2012 Challenge aimed at evaluating the respective merits and stages of development of the different computational techniques: direct numerical simulation (DNS), large eddy simulation (LES) and Reynolds averaged Navier Stokes (RANS) models. This study is an extension of our DNS analysis presented in the Challenge by Malm et al. [10] Some other relevant contributions were the assessment of vortical structures in the wake with LES by Shademan et al.,[11] the evaluation of the impact of the incoming boundary layer state carried out with LES by Chen et al. [12] and the compilation of turbulent statistics performed with DNS by Saeedi et al. [13]

The most widely used approach in industry is RANS due to its relative simplicity and reduced computational cost, although some standard RANS models are known to fail when computing geometries relatively different from the ones for which they were calibrated.[14] For instance, Wilcox [15] showed that the commonly used two-equation $k - \varepsilon$ model originally proposed by Launder and Spalding [16] performed well under ZPG TBL configurations, but failed when predicting boundary layers subjected to adverse pressure gradients. Even models with excellent performance in a variety of two-dimensional straight geometries such as the two-equation Shear Stress Transport (SST) model proposed by Menter [17] shows problems when computing highly three-dimensional and curved geometries,[18] characteristics which are often encountered in industrial flows. Along these lines, Uffinger et al. [19] used the $k - \varepsilon$ and the SST models to compute the flow around wall-mounted cylinders of various cross-sectional areas (including a square cylinder), and found significant discrepancy with their laser doppler velocimetry (LDV) measurements, even in mean flow quantities. Thus, one of the goals of using both DNS and LES to compute such complex flows, in addition to reaching deeper understanding of the physical mechanisms taking place, is to assess and further improve currently available tools for the industry. Possible ways of improving these models were discussed by Launder,[20] and other alternatives for a number of flow configurations are nowadays still under study.

A large number of studies have focused on the flow around the square wall-mounted cylinder of different aspect ratios (defined as the ratio between the cylinder height H and the square side d). It is an interesting case due to the number of different physical

phenomena taking place simultaneously: as the incoming flow approaches the obstacle, it faces a recirculation bubble formed on the windward side of the cylinder, which induces an adverse pressure gradient on the flow. This leads to a thickening of the incoming boundary layer, and transition in the resulting shear layer. Besides, a progressively widening horseshoe vortex is formed around the two sides of the cylinder, and the flow is accelerated close to the obstacle due to the favourable pressure gradient produced by the geometry. A massively separated wake is formed behind the obstacle, with a self-sustained oscillation process, and a downwash motion from the top of the cylinder is responsible for the widening of the wake. A case that has received some attention is the nominally two-dimensional square cylinder, i.e., a cylinder with square cross-sectional area and very large aspect ratio ($H \gg d$). This configuration has been studied both experimentally [21,22] and computationally [23,24] at low Reynolds numbers below $Re_d = U_\infty d/\nu = 500$ (where U_∞ denotes the freestream velocity and ν is the fluid kinematic fluid viscosity) in order to assess transitional effects in the wake and characterise the differences with respect to the circular cylinder. All these studies lead to a Strouhal number $St = fd/U_\infty$ (where f is the shedding frequency) of around 0.15–0.16 for this configuration, whereas the circular cylinder exhibits a larger Strouhal number of 0.2 as reported by Williamson.[25] Although the wake transition involves two modes of small-scale three-dimensional instability in both cases, modes 'A' and 'B', the square cylinder studies point out that both instabilities are found at Reynolds numbers different than in the circular cylinder case, and the spanwise lengths for two modes are also longer, which explains the lower Strouhal number. This is also connected to the differences in the separation process: whereas in a circular cylinder the separation occurs from a smooth surface, with varying location of the separation point in the azimuthal direction, in the square cylinder the upstream corners determine the separation point. With respect to studies focused on finite aspect ratio square cylinders, the experiments by Wang et al. [26] on a configuration of aspect ratio 5, at a higher Reynolds number of $Re_d = 11,500$, evaluated the effect of the incoming boundary layer on the wake. Interestingly, they found that thicker incoming boundary layers produced stronger spanwise vortices in the wake, leading to differences in its structure. Additional experiments by Wang and Zhou [27] and Wang et al. [28] on square cylinders of aspect ratios ranging from 3 to 7 led to lower Strouhal numbers, close to 0.1. This value is lower than the Strouhal number of 0.145 found by Hussein and Martinuzzi [29] in their LDV measurements of a wall-mounted square cylinder of unit aspect ratio, and this discrepancy is attributed to the different wake dynamics of this geometry.

The wind tunnel results used for the CFDSC 2012 Challenge, which were later compiled by Bourgeois et al.,[30] consist of particle image velocimetry (PIV) measurements combined with surface pressure sampling of a square cylinder of cross-sectional area d^2 and aspect ratio 4. The Reynolds number was $Re_d = U_\infty d/\nu = 11,000$. In the experiment the boundary-layer thickness at the middle of the cylinder but in its absence was reported to be $\delta_{99} = 0.72d$, which corresponds to a Reynolds number based on momentum thickness θ and freestream velocity of $Re_\theta \approx 1000$. The reported value for the freestream turbulence was 0.8%. Although there are currently available DNSs of ZPG boundary layers at Re_θ values of 4300 [7] and 6680,[8] here we show that the added complexity of the geometry poses a veritable challenge for any eddy-resolving numerical technique. Note that at this Reynolds number the large-scale flow is dominated by a von Kármán vortex street, in which vortices are shed at a well-defined Strouhal number in the turbulent wake. A wide spectrum of length scales (ranging from small turbulent structures in the shear layers to large vortices in the cylinder wake) is encountered, which constitutes an additional difficulty for the numerical method.

The aim of this work is to show that high-order spectral methods, which have tradition-ally been used with canonical cases, can also be applied to complex geometries closer to industrial applications. The flow under consideration in this study can be considered to be a'canonical complex geometry', since it is an external three-dimensional case with several physical phenomena playing an important role on the flow dynamics. These mechanisms, which involve transition, separation, shedding and pressure gradients, are very common in most industrial flows, and are very difficult to characterise properly with RANS-based simulations. In this study, we also show that accurate DNSs are also useful for assessing the quality of experimental set-ups, especially in terms of characterising initial and boundary conditions, which may significantly impact the resulting flow field.

As will be discussed in Section 2, we developed a numerical set-up which basically couples two computational codes to perform a DNS of the flow in the most efficient way. In Section 3, we show that the wakes obtained with the simulation driven by the laminar inflow and the one measured in the experiment showed noticeable differences, but they exhibited the same main vortex shedding frequency. This motivated an additional simulation, where a laminar-inflow condition was considered, in order to assess the impact of the state of the boundary layer on the main shedding. Comparisons between both simulations are also shown in Section 3, and the main conclusions of this study are summarised in Section 4.

2. Numerical method and simulation set-up

Since compressible effects are assumed to be small due to the relatively low velocities and lack of heat transfer, we solve the incompressible Navier–Stokes equations using the high-order spectral element code Nek5000, developed and maintained by Fischer et al.[31] It is important to highlight the fact that turbulent flows require high-order methods in order to properly resolve contributions from the smallest scales, which may significantly impact the final statistics. Nek5000 is based on the spectral element method (SEM) by Patera,[32] which combines the high accuracy of global spectral methods with the geometrical flexi-bility of finite element methods (FEM). The computational domain, sketched in Figure 1 in a spanwise-constant plane, is decomposed into K_{el} hexahedral spectral elements, where $K_{el} = 145, 744$ in the present simulation. Note that the horizontal coordinates are denoted by x (streamwise) and z (spanwise), and the vertical coordinate (parallel to the cylinder axis) is y. In each element, the governing equations are written in the weak form and discretised by a Galerkin projection, where test and trial functions are sought in different polynomial spaces $\mathbb{P}_N$ and $\mathbb{P}_{N-2}$ of maximum order N and $N-2$ for velocity and pressure, respectively, as discussed by Maday and Patera.[33] This results in a staggered pressure grid with regard to the velocity grid, obviating the appearance of spurious pressure modes. The solution of the instantaneous velocity $\tilde{\mathbf{u}} = (\tilde{u}, \tilde{v}, \tilde{w})$ is represented by tensor products of Lagrange polynomial interpolants $h_i^N(x)$ of order N. In a single element Ω^e, $e = 1, ..., K_{el}$, this approximation reads:

$$\tilde{\mathbf{u}}(\mathbf{x}^e(r, s, t))|_{\Omega^e} = \sum_{i=0}^{N} \sum_{j=0}^{N} \sum_{k=0}^{N} \tilde{\mathbf{u}}_{ijk}^e h_i^N(r) h_j^N(s) h_k^N(t), \tag{1}$$

where $\mathbf{x}^e$ is the coordinate mapping from the reference element $\hat{\Omega}$ to the local element Ω^e and $\tilde{\mathbf{u}}_{ijk}^e$ is the nodal basis coefficient. For the present simulation, we choose $N = 11$ for the velocity grid and $N = 9$ for the pressure grid, resulting in approximately 250 million velocity grid points. The simulation code Nek5000 considered in this study uses an
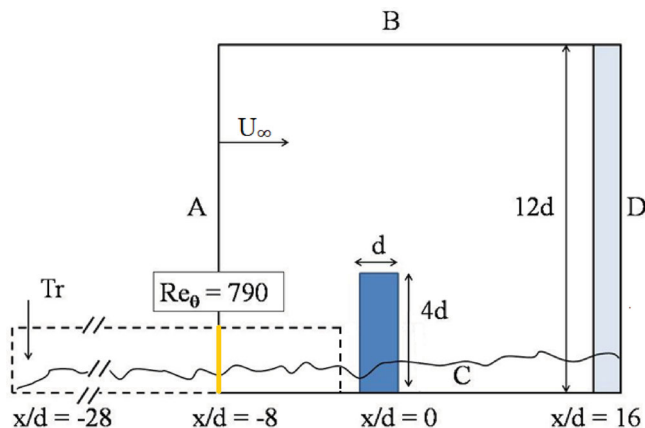
Figure 1. Simulation setup showing the domain where the flow around the cylinder is computed (solid). Data from the fully spectral precursor simulation (represented by the dashed domain) is provided as a time-dependent inflow condition at plane A. The interface between the two computational domains is highlighted in yellow, and the sponge region of length $2d$ upstream of the outlet is indicated by light blue color.

efficient parallelisation based on a message passing interface which has already been used in DNSs of flow configurations with millions of degrees of freedom.[34] The simulations were carried out on the AMD cluster 'Ekman'(using 2048 cores) and the CrayXE6 machine 'Lindgren' (using 4096 cores), both located at the PDC Center for Parallel Computers at KTH in Stockholm (Sweden). Excellent speedup on both architectures has been observed in a number of flow cases,[9,35] which is one of the main features of the code Nek5000.

2.1. *Numerical representation of the experimental set-up*

In the reference experiment, the leading edge of the flat plate where the zero boundary layer developed was reported to be $16d$ upstream of the cylinder. In order to reduce computational cost, the numerical domain where the flow around the cylinder is solved does not extend all the way up to the leading edge of the flat plate, but only up to a distance $8d$ upstream of the cylinder. This is indicated in Figure 1 by the solid rectangle with sides A, B, C and D. On the other hand, the inflow condition for the main computation is obtained from another simulation of a ZPG boundary layer performed with the more efficient (but geometrically less flexible) Fourier–Chebyshev spectral code SIMSON,[36] which generates time-dependent Dirichlet inflow conditions ahead of the main simulation. Note that this strategy synergistically combines the best features from both codes: SIMSON is able to compute simple geometries very efficiently thanks to the use of Fourier expansions in both homogeneous directions (streamwise and spanwise), but is limited to Cartesian geometries and to a Gauss–Lobatto–Chebyshev node distribution in the inhomogeneous wall-normal direction. On the other hand, Nek5000 is not as efficient due to the more general formulation of the governing equations and the need to perform costly matrix products, but has fewer limitations in terms of geometry since one has the freedom to choose the location of the spectral elements (only the distribution of Gauss–Lobatto–Legendre nodes within each element is prescribed) while maintaining spectral accuracy.
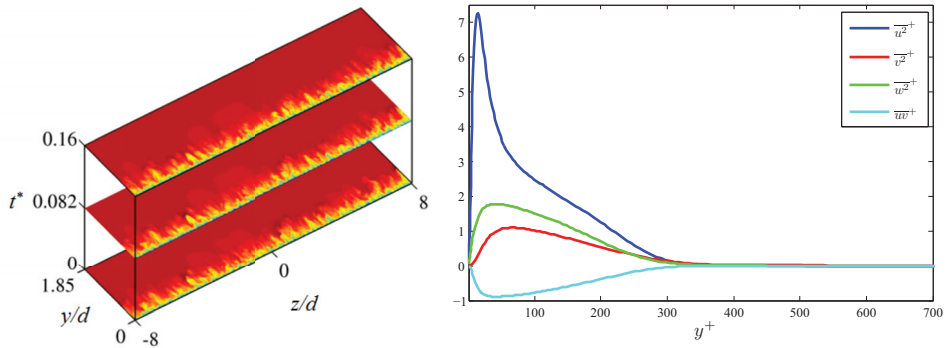
Figure 2. (Left) Time-dependent inflow condition for instantaneous streamwise velocity ũ at three different instants from the auxiliary ZPG boundary layer computation carried out with SIMSON. Data extracted at $x/d = -8$, and values range from 0 (blue) to 1 (red). Third order Lagrangian interpolation in time between two given planes of data is performed every time-step. (Right) Time-averaged normal and shear stresses of the boundary layer computed at $x/d = -8$ in the SIMSON domain.

The domain corresponding to the SIMSON simulation is indicated by the dashed rectangle in Figure 1: it starts with a laminar Blasius profile at $x/d = -28$ ($Re_\theta = 180$), spans a downstream distance of $33d$ and ends at around $Re_\theta = 1000$. Note that the cylinder is not part of this domain, and only a standard ZPG boundary layer is solved, in a very similar set-up to the ones by Schlatter et al. [37] or Schlatter and Örlü.[7] The domain of the precursor simulation is discretised using $1024 \times 201 \times 768$ grid points in the streamwise, wall-normal and spanwise directions, respectively. Transition to turbulence is triggered by means of a trip-forcing technique approximately at the location of the arrow in Figure 1, indicated by 'Tr'. This technique was successfully employed in previous spatially developing boundary-layer simulations from our research group [7,37]. The auxiliary simulation is designed to produce the correct boundary-layer thickness $\delta_{99} = 0.72d$ at $x/d = 0$, as measured in the experiment. Note that in the experiment the flat plate starts $16d$ upstream of the obstacle, and a sharp leading edge flat plate is used to produce the TBL; the simulated boundary layer, on the other hand, is tripped $28d$ upstream of the obstacle.

The interface between the two simulations is highlighted in Figure 1 on plane A: the velocities from the SIMSON simulation at $x/d = -8$ (which corresponds to $Re_\theta = 790$) are stored every 0.08 convective time units (where the non-dimensional time t^* is obtained in terms of the freestream velocity U_∞ and the square side d), and are interpolated in space to match the SEM grid from the main computational domain, as shown in Figure 2 (left) with a series of three fields. During the main simulation, third-order Lagrangian interpolation is performed at every time-step between the two stored planes of data to obtain the inflow boundary condition applied on A in Figure 1. Figure 2 (right) shows the time-averaged normal and shear stresses of the boundary layer computed at $x/d = -8$ in the SIMSON domain, and used as inflow condition for the main simulation. These profiles, together with the mean flow shown below in Figure 3 (middle), highlight the quality of the incoming boundary layer in the turbulent-inflow case. It is important to note that the method described here represents an improvement with respect to the so-called recycling techniques (see for instance the work by Lund et al. [38]), since the auxiliary simulation provides a sufficiently long time history of the inflow so that any unphysical behaviour due to an artificial recycling frequency is avoided. In addition to this, the boundary-layer
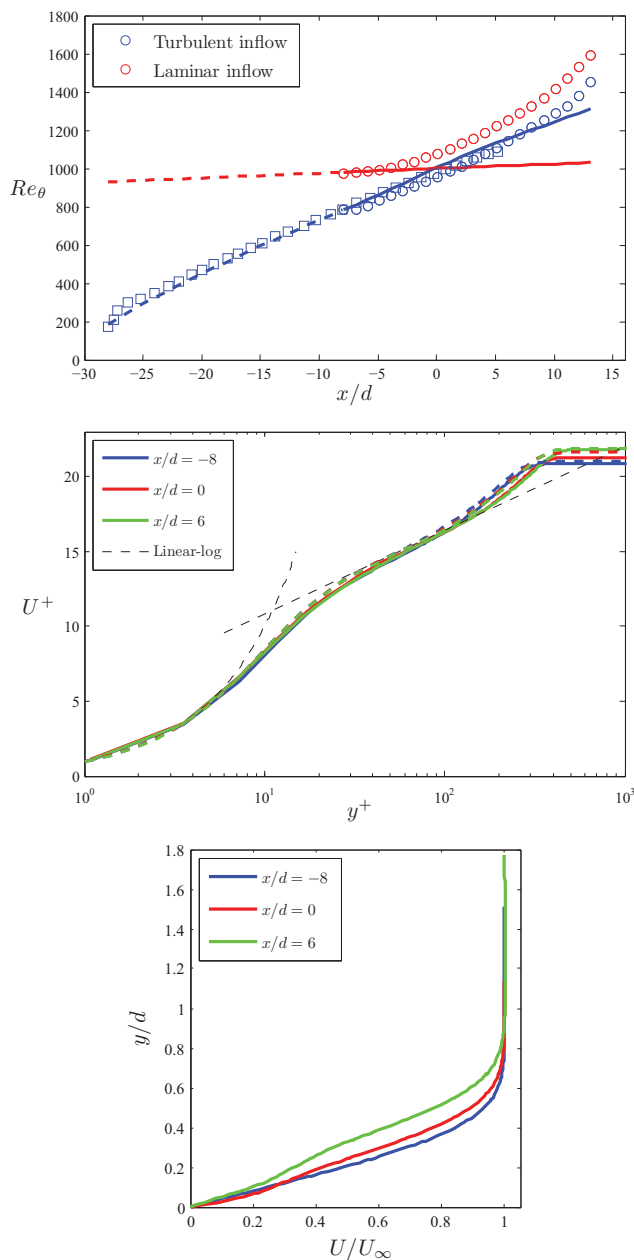
Figure 3. (Top) Time-averaged Reynolds number based on momentum thickness Re_θ for both simulations, together with reference trends [41] denoted by solid (Nek5000 domain) and dashed (SIMSON domain) lines. Circles correspond to the values obtained in the Nek5000 domain, whereas squares represent values computed in the SIMSON domain. (Middle) Inner-scaled mean velocity profiles at three positions given in the Nek5000 frame of reference. Solid lines represent turbulent-inflow profiles computed in the Nek5000 domain, and dashed lines correspond to profiles obtained in the SIMSON domain. Linear and logarithmic laws, with $\kappa = 0.41$ and $B = 5.2$ [42], are also shown. (Bottom) Outer-scaled mean velocity profiles obtained from the laminar-inflow simulation at the same three locations.

and the main cylinder simulations are not coupled, and therefore no spatial correlations or artificial frequencies will appear (Herbst et al. [39]).

The numerical problem is completely defined by the application of no slip conditions at the wall C shown in Figure 1 as well as the surfaces of the square cylinder, periodic boundary conditions in the spanwise direction (z), and no-stress conditions at the top boundary B and at the outflow D. These boundaries are located $12d$ above the lower wall and $16d$ downstream of the obstacle, as indicated in Figure 1, and the spanwise width of the computational domain is $16d$. Note that according to the PIV measurements by Wang and Zhou [27] on a square cylinder of aspect ratio 7 at $Re_d = 9300$, the dimensions of the computational domain are adequate to confine and compute accurate statistics of the wake produced in this configuration. A thin sponge region of length $2d$ upstream of the outlet at D creates a disturbance-free outflow, ensuring numerical stability (see for instance [40]). In this region, the flow is forced to the spanwise mean flow given at the present time, which guarantees the correct mass flux.

With respect to the laminar-inflow case, only the main simulation domain is considered, and we fix the inflow boundary condition to a laminar profile defined by the Blasius similarity solution that would yield a boundary layer with $Re_\theta = 1000$ at $x/d = 0$ if there was no obstacle. To this end, a Blasius profile with $Re_\theta = 975$ is imposed on plane A as defined in Figure 1. Note that this higher value of the Reynolds number at the inflow plane compared to the turbulent-inflow is due to the slower spatial growth of the laminar Blasius boundary layer.

2.2. *Streamwise development of the incoming boundary layers*

The streamwise development of both boundary layers in the Nek5000 domain, together with the quality of the inflow conditions provided by the precursor simulation with SIMSON, are discussed next. Figure 3 (top) shows the Reynolds number based on momentum thickness Re_θ as a function of the streamwise coordinate for both computational domains. The following reference streamwise evolutions are shown for comparison (Schlichting [41]):

$$Re_{\theta,\text{lam}}(x) = \frac{0.664\, x}{\sqrt{Re_x}} \frac{U_\infty}{\nu}, \tag{2}$$

$$Re_{\theta,\text{turb}}(x) = \frac{0.036\, x}{Re_x^{1/5}} \frac{U_\infty}{\nu}, \tag{3}$$

where in both cases Re_x is the Reynolds number based on freestream velocity and streamwise coordinate x. In the laminar-inflow case, the condition $Re_\theta(x = 0) = 1000$ yields a boundary-layer origin $x_{0,\text{lam}} \simeq -206.2$, where in the turbulent case a 'virtual origin' $x_{0,\text{turb}} \simeq -32$ is obtained. Note how both equations cross at $x/d = 0$ with the required value of $Re_\theta = 1000$. The values obtained from the simulations in the Nek5000 domain are computed by averaging profiles between $z/d = \pm 7.5$ and ± 8 in time. The flow in this region was initially assumed to be undisturbed by the effect of the obstacle, although as discussed below this will not be completely true, especially in the laminar-inflow case. The values computed from both simulations at $x/d = 0$ are $Re_\theta \simeq 955$ and 1077, which are close to the target value of 1000 with relative errors below 8%. Also, a boundary-layer thickness of $\delta_{99} \simeq 0.71d$ is obtained in the turbulent-inflow case, in very good agreement with the value reported by Bourgeois et al. [30] of $\delta_{99} \simeq 0.72d$, and slightly larger than the laminar-inflow case ($\delta_{99} \simeq 0.64d$). This is all consistent, since the goal was to match Reynolds number based

on momentum thickness at the obstacle, and therefore the TBL is thicker than the laminar one. In the laminar-inflow case, the streamwise development agrees well with Equation (3) for both Nek5000 and SIMSON simulations, although it is interesting to observe how in the Nek5000 domain the computed values start to deviate from the expected trend for $x >$ 10d. This is due to the progressively spreading wake behind the obstacle, which eventually interacts with the boundary layers even very close to $z/d = \pm 8$. Interestingly, the laminar-inflow simulation shows deviations with respect to the expected trend (2) much earlier, at $x/d \simeq 0$, which is the location of the cylinder. This is due to the fact that, as discussed in Section 3.2, the horseshoe vortex formed in the laminar case is wider than the turbulent one. This suggests that the computational domain may not be wide enough to completely avoid confinement effects close to $z = \pm 8d$, although in Section 3, we argue that the domain width is adequate to properly capture the physics of both wakes, which is the main focus of this study.

Figure 3 (middle) confirms the existence of confinement effects in the turbulent-inflow simulation, reflected on the inner-scaled mean velocity profiles at three different streamwise locations, which roughly correspond to $Re_\theta \simeq 790$, 955 and 1140 in the laminar-inflow simulation. These profiles are compared with the ones obtained with SIMSON at the same streamwise locations, and although both sets of data properly represent the viscous and log layers, slight deviations can be observed in the wake region. Note that in both simulations the mesh was designed so that the first gridpoint above the wall is located below $y^+ = 1$. Figure 3 (bottom) shows the outer-scaled mean velocity profiles from the laminar-inflow simulation at the same three locations. In this figure, the effects of confinement become more noticeable from $x/d = 0$ to 6. With respect to the inner-scaled streamwise turbulence intensities at the same locations (not shown), some discrepancies with respect to the reference data exist around the peak of $\overline{u^2}^+$ and the wake regions in the laminar-inflow case. This could be attributed to the resolution in the near-wall region, which in the Nek5000 domain was slightly lower than for the reference DNS data for TBLs.[7] On the other hand, the laminar-inflow simulation exhibits a very subtle build-up of turbulence intensity at $x/d = 0$, which progressively increases at $6d$ due to the transition induced by the horseshoe vortex formed around both sides of the cylinder.

3. Results

3.1. *Comparison of instantaneous flow fields*

After assessing the flow development of both boundary layers, in this section we compare the most significant flow features exhibited by the two simulations. Figure 4 shows instantaneous velocity fields for both cases at $t^* \simeq 100$ after the beginning of the simulations, represented by isosurfaces of the streamwise velocity component equal to 10% of the freestream velocity. Note that $t^* = 0$ would correspond to the beginning of the main simulation, which is initiated after discarding the initial transients in the precursor simulation with SIMSON. Transient effects are observed in the main simulation up to $t^* \simeq$ 55, and both cases were run for over 100 additional convective time units, i.e., more than 10 shedding periods. This figure shows the most relevant physical phenomena in the flow, and how they differ according to the inflow conditions. For instance, the thickening of the incoming boundary layer due to the adverse pressure gradient formed at the obstacle can be observed in both cases, although the recirculation bubble is significantly larger in the laminar-inflow case. In this case, it is also interesting to note how the adverse pressure gradient produces instabilities in the incoming laminar boundary layer which eventually lead to
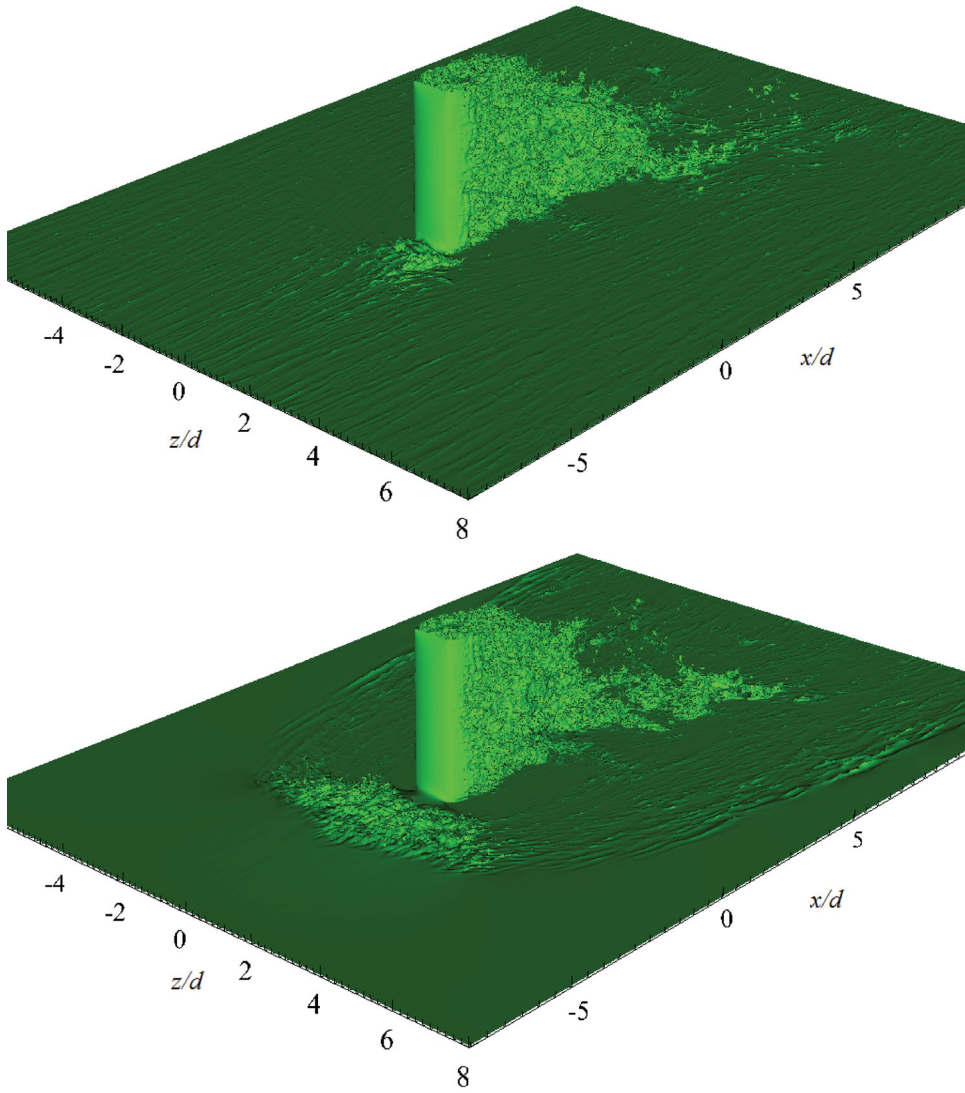
Figure 4. Isosurfaces of instantaneous streamwise velocity $\tilde{u} = 0.1 U_\infty$ corresponding to (top) turbulent and (bottom) laminar-inflow cases, both at $t^* \simeq 100$ from the beginning of the simulation.

transition. The flow behind the cylinder is massively separated and exhibits a self-sustained oscillation in both cases, as well as large areas of reversed flow will be discussed below. Of special relevance for understanding differences between both states of the boundary layer is the shape of the wakes as well the evolution of the individual structures throughout its shedding. With respect to the results shown in Figure 4, it is interesting to note how both simulations capture, with a great degree of detail, the occurrence of near-wall streaks: in the laminar-inflow case streaks exhibit the characteristic spanwise spacing $\Delta z^+ \simeq 100$ in the regions where a nominally ZPG TBL is encountered, i.e., the areas of the domain not affected by the obstacle. In the laminar-inflow simulation streaks appear after the obstacle is reached, which indicates transition to turbulence, although they do not exhibit such a

structured pattern as in the turbulent simulation due to transitional effects and the more pronounced influence of the cylinder. Also note how the wide horseshoe vortex formed around the cylinder clearly disturbs the flow even close to $z/d = \pm 8$, which explains the deviation from empirical relations observed in Figure 3.

Streaks observed in the turbulent-inflow simulation appear straight and undisturbed at the spanwise centreplane approximately up to around $4d$ ahead of the obstacle. After this point they are slightly bent and deflected due to the presence of the cylinder, as can also be observed in Figure 5 (top) where an instantaneous streamwise velocity field is shown at $y^+ \simeq 15$ (wall units are determined from the turbulent-inflow case, and this position corresponds to $y = 0.027d$). Figure 5 also shows that at a spanwise distance of approximately $6d$ from the cylinder the streaks are straight and the boundary layer is relatively undisturbed. Upstream of the cylinder the flow stagnates, which gives rise to a thickening of the incoming boundary layer as can also be observed in Figure 4 (top). Transition to turbulence takes place in the thin shear layers on the sides and the top of the cylinder that bound the separation bubbles on these surfaces. It is interesting to note that in the laminar-inflow simulation, streaks appear only downstream of the obstacle, and at spanwise distance larger than $4d$ from the centreplane, as shown in Figure 5 (bottom). This can also be observed in the instantaneous visualisation provided in Figure 4 (bottom), which in addition shows that the horseshoe vortex can be clearly identified even in the instantaneous fields, unlike in the turbulent-inflow simulation where it is only visible after timeaveraging (as will be discussed below). This was also observed experimentally by Nagib and Corke,[4] who performed smoke-wire visualisations of the flow around square cylinders of different aspect ratios under various inflow conditions. Figure 5 (bottom) also shows that at $x/d \simeq 0$, the region very close to the cylinder is significantly disturbed (up to around $z/d \simeq 3$), and then there is a second region, up to $z/d \simeq 6$, which is less disturbed by the obstacle. This is a consequence of the complex transitional mechanisms taking place in this region, which are also affected by local pressure gradient effects and curvature of the streamlines. In both cases, the point of separation on the cylinder is fixed to the sharp upstream edges (two vertical and one horizontal), thereby falling into the category of so-called 'geometry-induced' separation.

An interesting difference between the instantaneous wakes from the two simulations can be observed in Figure 6, where the streamwise velocity extracted at $y \simeq 2d$ (above both boundary-layer edges) is shown for both cases 100 convective time units after the beginning of the simulations. Instantaneously, both wakes have a similar half-width Δ_w of around $0.8d$ right after the obstacle, up to $x \simeq 2.6d$. However, as one moves downstream the turbulent wake becomes wider than the one in the laminar-inflow simulation, reaching its maximum half-width of around $4d$ at $x \simeq 13d$, compared with the half-span of the laminar-inflow case of approximately $3d$.

3.2. *Comparison of time-averaged flow fields*

Although in Section 3.1 it is shown that the wake from the turbulent-inflow simulation is instantaneously wider than the one from the laminar-inflow case for $x > 2.6d$, the time-averaged flow fields reveal that the latter is slightly wider than the former for $x > 3d$. This can be observed in Figure 7, where the respective half-widths of both cases are shown for wall-normal locations ranging from $y/d = 1$ to 4. Here we estimate the location of the wake edge at each location as the point where the streamwise velocity is $0.99U_\infty$. The wakes from the two simulations exhibit the same Δ_w up to $x \simeq 3d$ at all wall-normal locations, and after this point some differences start to appear. The $y/d = 1$ curve shows an interesting trend, where
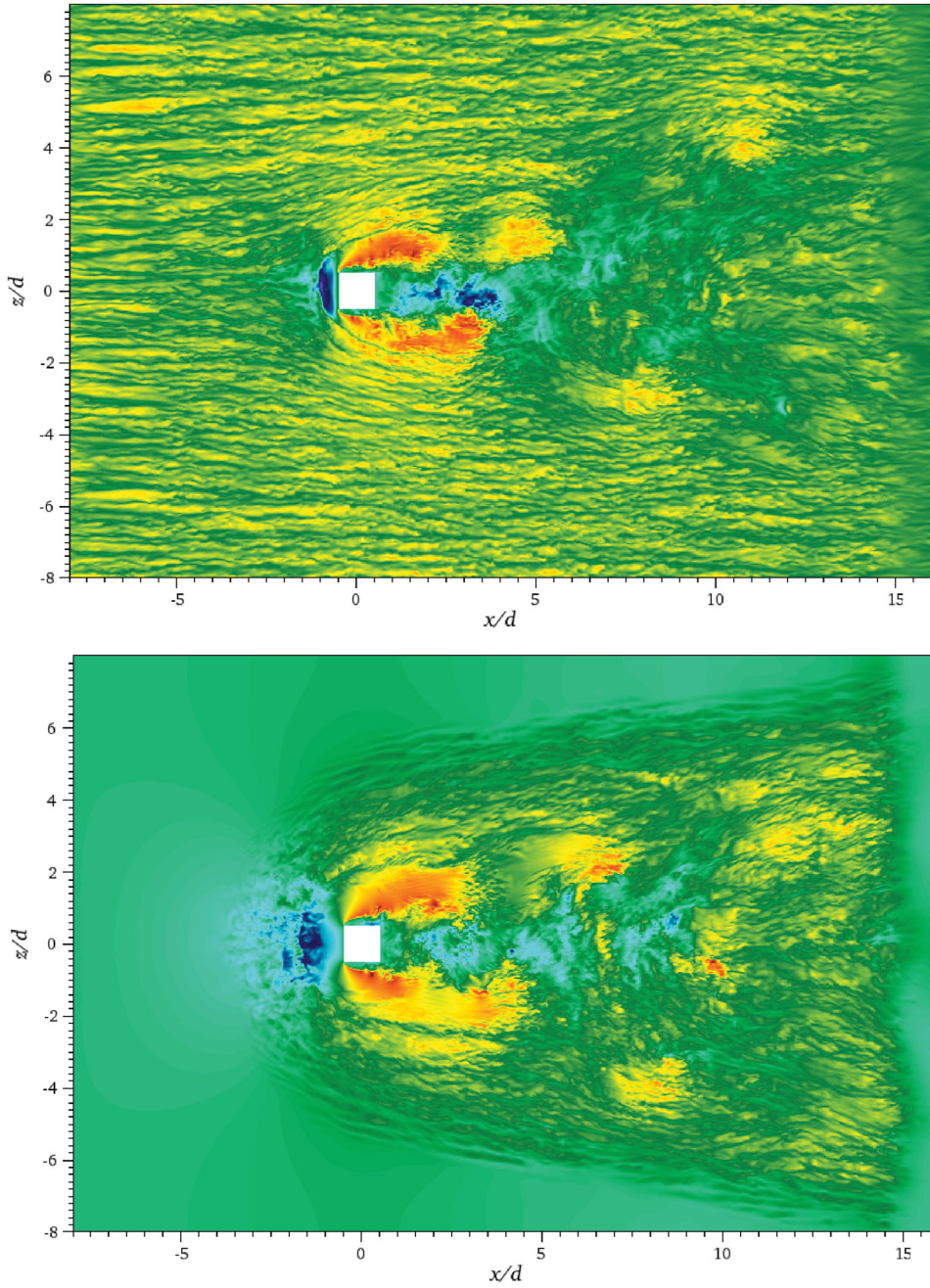
Figure 5. Streamwise velocity fields normalized with U_∞ at $y^+ \simeq 15$ corresponding to (top) turbulent and (bottom) laminar-inflow simulations, extracted after 100 convective time units. Note that wall units were determined from the time-integrated turbulent-inflow profile, and this location corresponds to y = 0.027d. Velocities range from -2 (dark blue) to $+2$ (dark red). Also note the presence of the sponge region between $x/d = 14$ and 16.
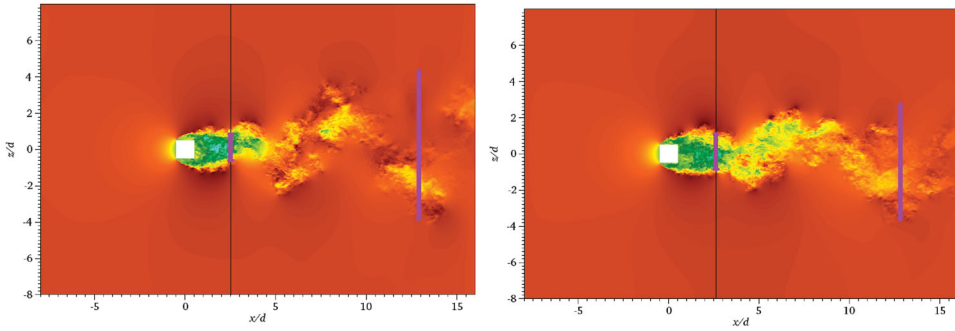
Figure 6. Streamwise velocity fields normalized with U_∞ at $y \simeq 2d$ corresponding to (left) turbulent and (right) laminar-inflow simulations, extracted after 100 convective time units. The two wakes exhibit similar features up to $x/d = 2.6$, location which is indicated by thin black lines. Thick magenta lines give estimations of the wake width at $x/d \simeq 2.6d$ and 13. Velocities range from -2 (dark blue) to $+2$ (dark red). Also note the presence of the sponge region between $x/d = 14$ and 16.

the laminar-inflow wake is slightly narrower than the turbulent-inflow one up to $x = 7d$, and after this point it becomes 25% wider due to the interaction with the spreading horseshoe vortex downstream of the obstacle. With respect to $y = 2d$, both wakes exhibit similar widths and growth rates up to $x = 3d$, the location after which the laminar-inflow case shows a wake around 10% wider than the turbulent-inflow one. Also note how as the distance from the wall y increases the wakes become narrower, which as will be discussed below is a consequence of reduced momentum transport (a wall-normal distance equal
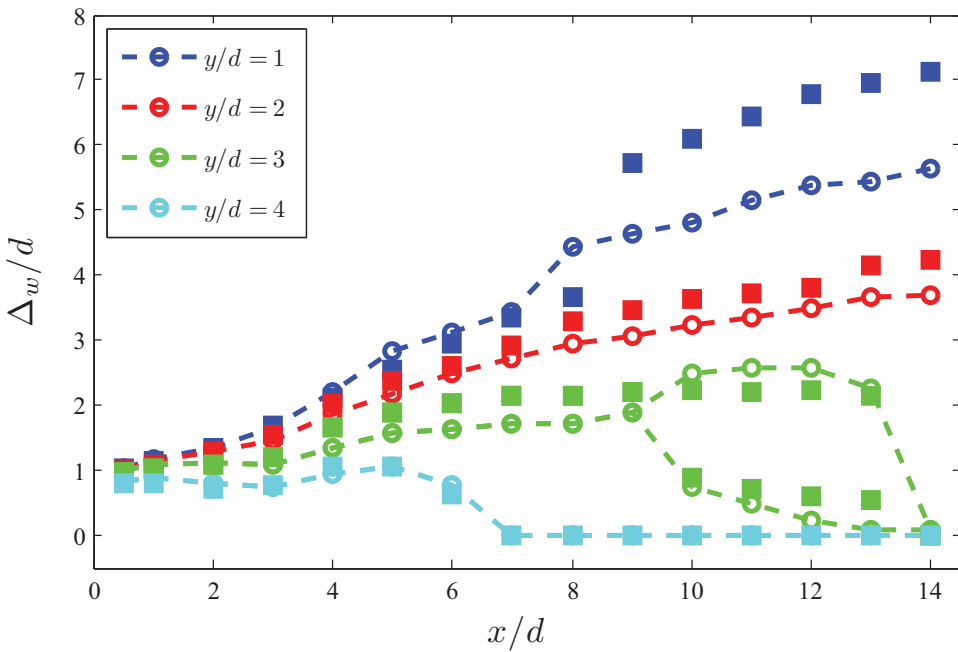

Figure 7. Half-width of the wake Δ_w as a function of the streamwise position x, for various wall-normal locations y. Open circles with dashed lines correspond to the turbulent-inflow simulation, whereas filled squares represent values from the laminar-inflow case.
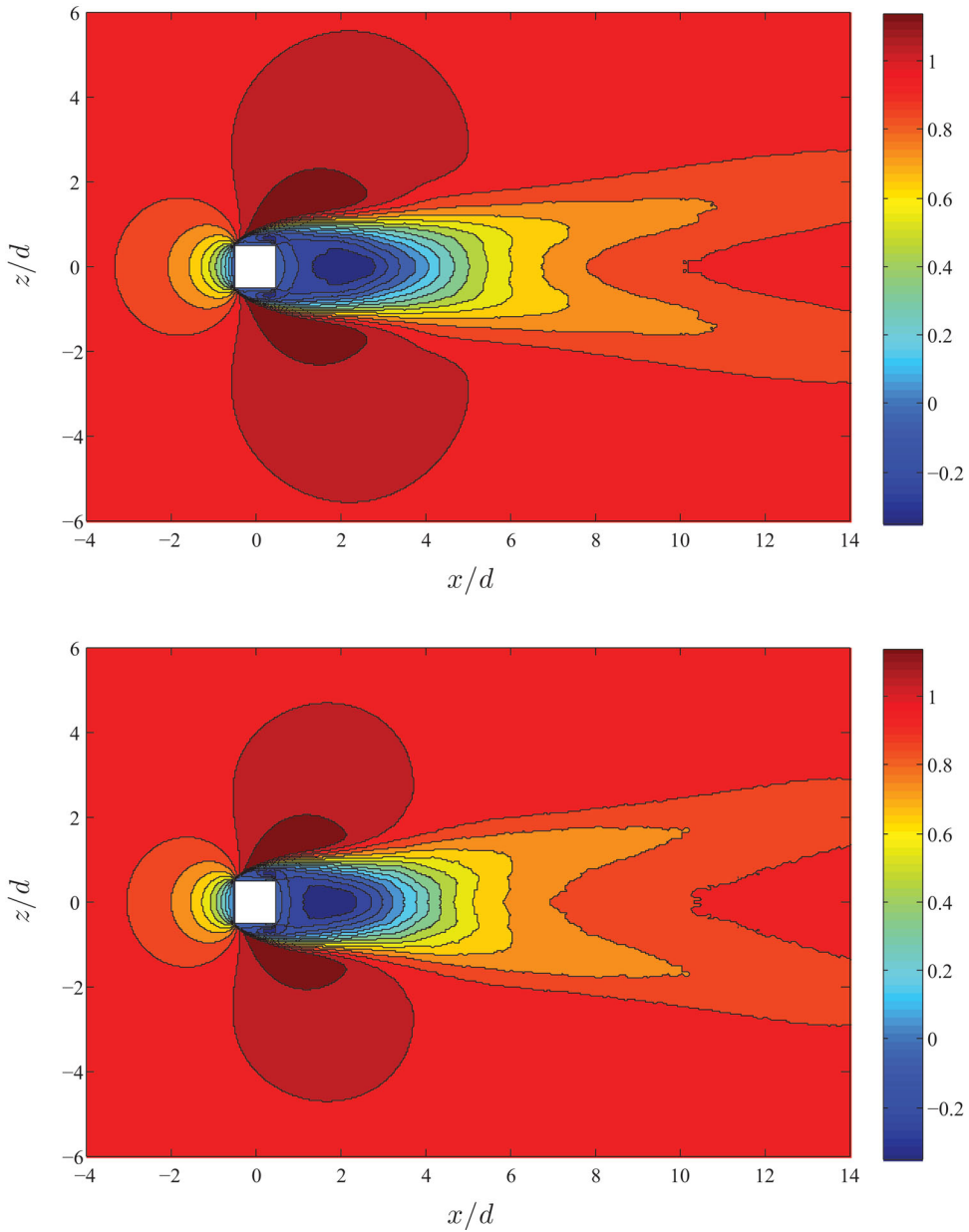
Figure 8.　Time-averaged streamwise velocity fields U normalized with U_∞ at $y \simeq 2d$ corresponding to (top) turbulent and (bottom) laminar-inflow simulations.

to $2d$ approximately corresponds to three times the boundary-layer thickness before the obstacle). The mean streamwise velocity at $y = 2d$ is shown in Figure 8, where the slightly larger spreading of the laminar case becomes noticeable as one moves downstream. The very similar features of both wakes for $x < 3d$ are also noticeable in this figure, which also shows how the flow accelerates around the two sides of the cylinder due to the favourable pressure gradient induced by the geometry. The effect of the stagnation point in front of the

obstacle disturbing the incoming flow, which as discussed below is actually located close to $y = 2d$ in both cases, can also be noticed in this figure. A time-averaged visualisation of the flow field (not shown) also reveals that the turbulent wake shows a more organised turbulent structure than the laminar one, due to the fact that a boundary layer with fullydeveloped turbulent features was the incoming flow, whereas in the laminar case characteristics of transitional flows still remain visible. The $y = 3d$ trend once again shows how the two wakes start to exhibit different widths after $x \simeq 3d$, with the turbulent-inflow one showing around 20% more span. An interesting phenomenon takes place in Figure 7 at $x = 10d$: both the turbulent and the laminar-inflow curves split into two parts, which eventually meet at $x = 14d$ with zero width. This phenomenon, which can be observed in more detail in Figure 9, is due to the formation of two regions in the wake: a narrower core section and two additional tails on both sides. If one defines the wake edge as the last point in z where the streamwise velocity is $0.99U_\infty$, then the split in Figure 7 disappears, and only the upper part of the curve would be considered. It is also interesting to connect this figure with the $y = 2d$ field, which shows two different tails: this is a manifestation of the transition from the near-wall flow highly influenced by the boundary layers on both sides, towards the progressively more irrotational flow at the freestream. Also in this configuration the two wakes are very similar for $x < 3d$, and only farther downstream the effect of the obstacle is less dominant. Finally, the $y = 4d$ curve (which is at the same level as the top of the cylinder) shows very good agreement between the two wakes, revealing that any effect from the different flows penetrating from the sides does not impact the wake at this location. Also, the wake is much shorter at this location: it starts to reduce its width at $x = 5d$, and extends up to $x = 7d$. Beyond this wall-normal position, the flow is essentially uniform.

The fact that the two wakes are so similar up to around $x \simeq 3d$ can be further explained by the fact that the geometry determines the separation point due to the sharp corners encountered by the flow. Therefore, and as will be discussed below, the state of the incoming boundary layer does not influence the separation process or the vortex shedding frequency in the von Kármán street, which is essentially the same in both cases. However, after a distance of around $3d$ the wake mixes with the incoming flow on the two sides of the obstacle, therefore leading to different characteristics depending on the local turbulence level. This can be observed in Figure 10, where the Reynolds shear stress $\overline{uv}$ is shown at the centreplane of the domain ($z/d = 0$) for both turbulent and laminar-inflow cases. The two fields look qualitatively similar for $x < 3d$, and after this point the laminar-inflow case shows a region of strong positive $\overline{uv}$ which goes from $y \simeq d$ up to $y \simeq 2d$, forming an angle of $\simeq 30°$ with respect to the streamwise axis. This indicates more efficient wall-normal transport, characteristic of turbulent flows, and interestingly in the laminar-inflow case this region is almost parallel to the flow, which is a characteristic of flows closer to a transitional stage in the wake. This also explains why the region of intense $\overline{uv}$ extends farther downstream in this configuration. Horizontal planes of $\overline{uv}$ are very similar close to the wall, although at $y^+ \simeq 100$ (within the logarithmic region) the turbulent flow case exhibits higher values of the Reynolds shear stress, especially past $3d$ downstream of the cylinder.

The main reason for the instantaneously wider wake in the laminar-inflow case is inferred from Figure 11, where the root-mean-squared (rms) spanwise turbulence intensity w_{rms} is shown at the centreplane for both cases. Here it is clear that, even if very close to the wall the spanwise fluctuations are more intense in the laminar-inflow case, for $x > 3d$ the turbulent-inflow case exhibits more intense fluctuations above $y = 2d$, which contribute to the widening of the wake. As reported by Zdravkovich [2] and by Wang and Zhou,[27] the wake shows higher velocities far from the wall due to the downwash flow
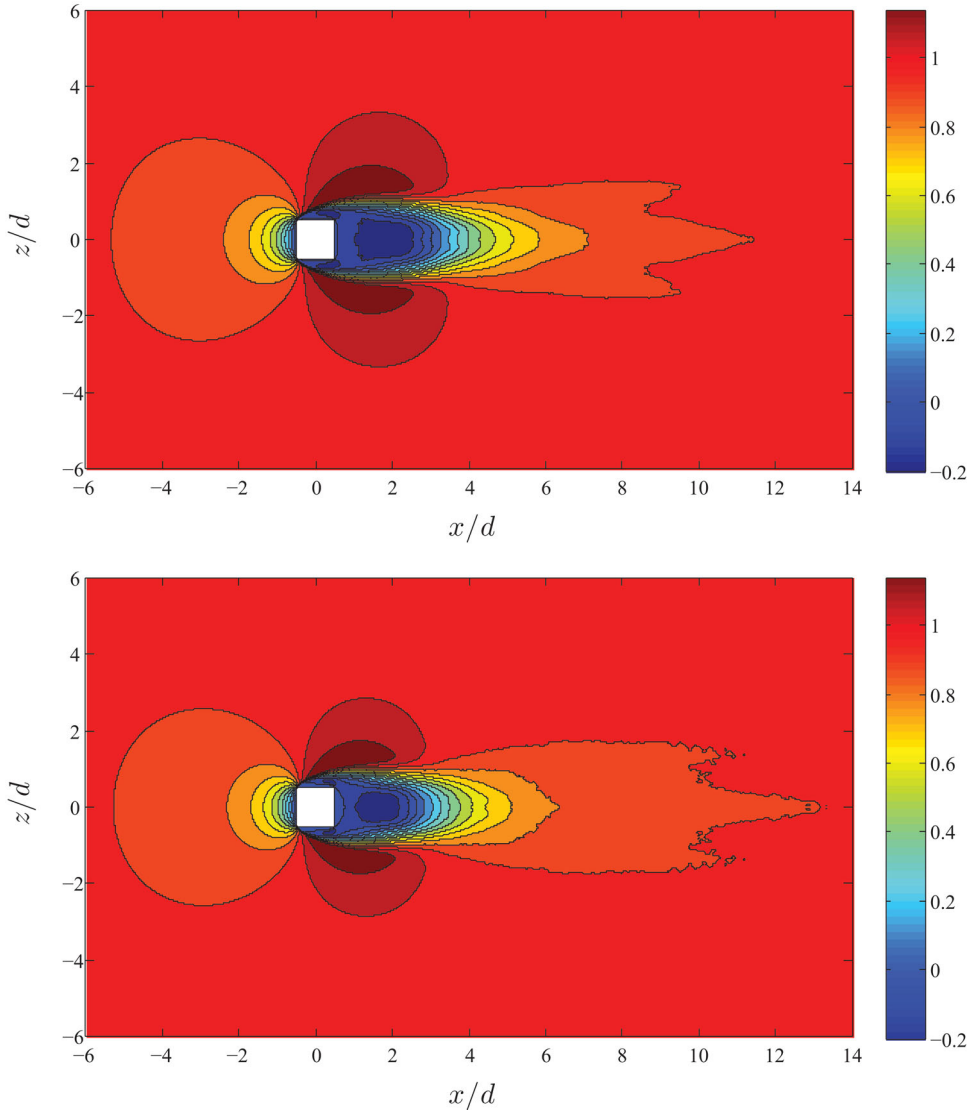
Figure 9.   Time-averaged streamwise velocity fields U normalized with U_∞ at $y \simeq 3d$ corresponding to (top) turbulent and (bottom) laminar-inflow simulations.

from the top of the obstacle, which is the main agent contributing to the spanwise widening of the wake. Note that the instantaneously wider turbulent-inflow wake is also in agreement with the experiments by Wang et al.,[26] who reported that thicker incoming boundary layers lead to stronger spanwise vortices in the wake.

   As observed in Figure 8, the flow accelerates on both sides of the cylinder due to the favourable pressure gradient induced by the geometry. As discussed above in conjunction with Figure 4, the streamwise streaks are suppressed in this region, although as reported by Piomelli et al. [43] in favourable pressure gradient boundary layers the streaks appear to be less wiggly and more elongated, but not necessarily weaker. The pressure gradient acting on the boundary layers on both sides of the cylinder can be characterised by the acceleration
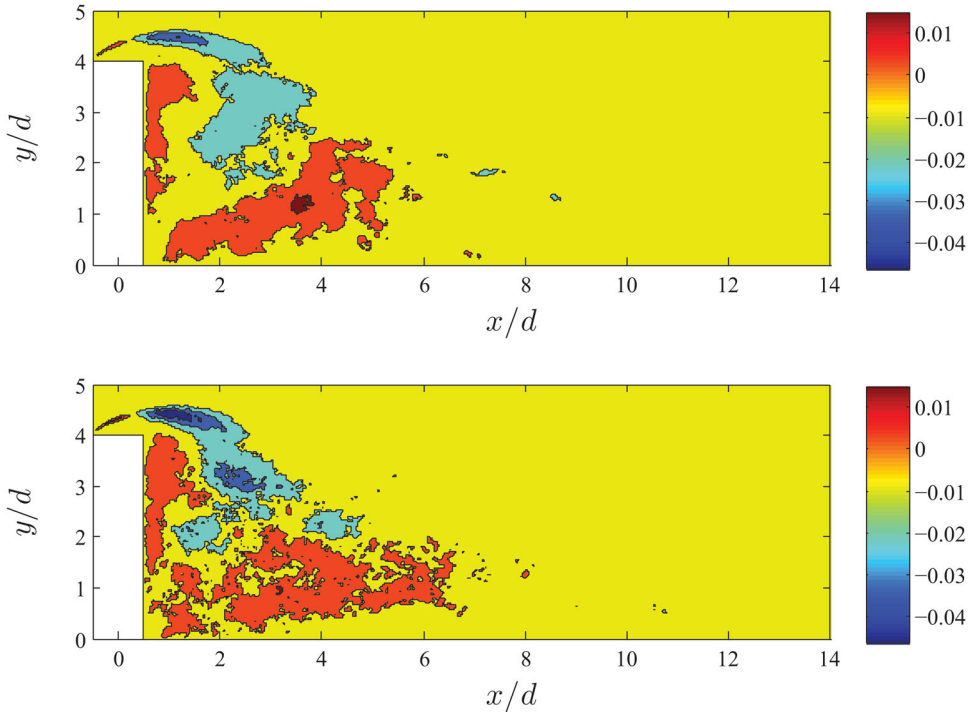
Figure 10.   Time-averaged Reynolds shear stress fields $\overline{uv}$ normalized with U_∞^2 at $z/d = 0$ for the (top) turbulent and (bottom) laminar-inflow simulations.

parameter K, defined as follows:

$$K = \frac{\nu}{U_\infty^2}\frac{\mathrm{d}U_\infty}{\mathrm{d}x}, \tag{4}$$

where U_∞ is the local freestream velocity in Equation (4). Piomelli et al. [43] argue that if a boundary layer is subjected to a sufficiently strong favourable pressure gradient ($K \geq 3 \times 10^{-6}$) for long enough distances, relaminarisation may occur. In fact, as the boundary layer accelerates the Reynolds number decreases, and the flow is considered to be relaminarised if Re_θ decays below some critical value between 330 and 400 depending on flow conditions. Taking as reference the planes located at $z = \pm 1.5d$, the acceleration parameter takes the values $K \simeq 2 \times 10^{-5}$, 5×10^{-6} and 2.4×10^{-6} at $x/d = 0.5$, 1 and 2, respectively. The lowest Re_θ value, 738, is obtained at $x = 2d$. Therefore, a trend towards relaminarisation is observed, although the local Reynolds number is above the critical value because the pressure gradient affects the flow for a relatively short distance, in the order of only 3 boundary-layer thicknesses (which roughly corresponds to 24 displacement thicknesses δ^* [41]). In the study by Piomelli et al.,[43] K values larger than 3×10^{-6} acted on the flow for at least $100\delta^*$, and they obtained a minimum Re_θ slightly above 400. However, even if they came closer to the limit of relaminarisation, they did not observe attenuation in the intensity of their near-wall streaks. Note that an additional factor present in this case is the local curvature of the streamlines induced by the geometry, which was not present in the simulations by Piomelli et al. and could also contribute to the attenuation of the streaks.
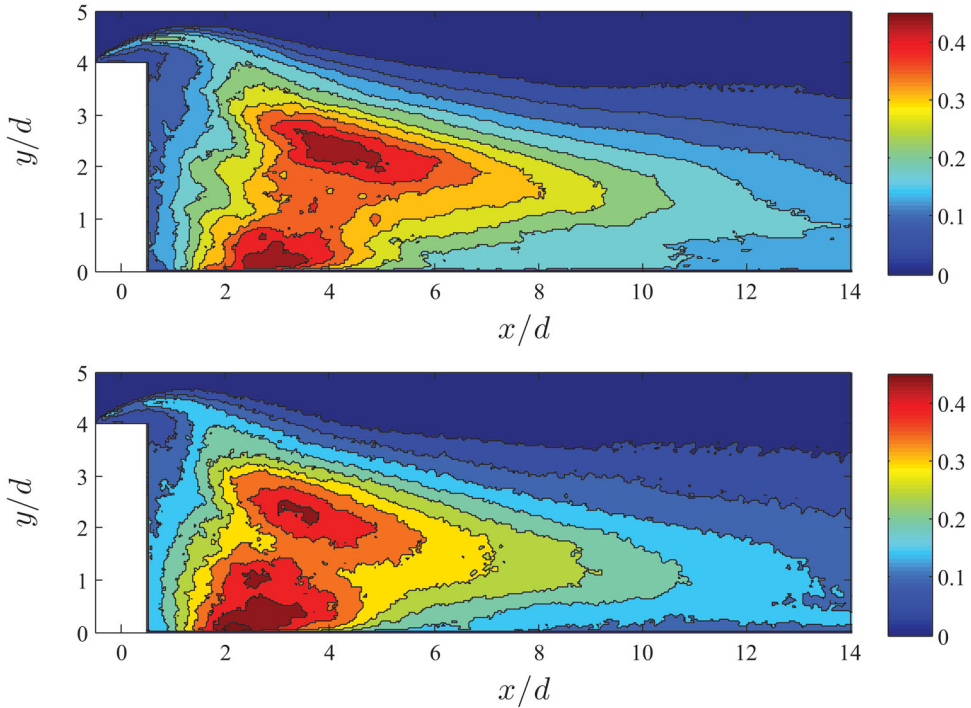
Figure 11. Spanwise turbulent intensity fields w_{rms} normalized with U_∞ at $z/d = 0$ for the (top) turbulent and (bottom) laminar-inflow simulations.

Another finding by Piomelli et al. [43] was the fact that under the influence of a favourable pressure gradient the ratio of the streamwise to the spanwise turbulence intensities $\overline{u^2}/\overline{w^2}$ significantly increased close to the wall, which explains the more elongated and less wiggly streaks. Interestingly, this is not the case along the sides of the cylinder, as can be observed in Figure 12, where u_{rms} is shown for both simulations at a spanwise section $1.5d$ apart from the centreplane of the domain (these fields are the average of the mean fields at $z = +1.5d$ and $-1.5d$). The streamwise turbulence intensity is very low at $x/d \simeq 0$, i.e., in the region affected by the accelerating pressure gradient, even in the laminar-inflow case. This explains the fact that the streaks are much weaker in this area, and raises the question of why this component of the fluctuations is also attenuated, in contrast with what was observed by Piomelli et al. [43]. This figure also reveals an interesting two-layer structure of the laminar-inflow wake: at $x \simeq 5d$ a peak is observed close to the wall, and another one at $y \simeq 2d$. This is not observed in the turbulent-inflow case and is a manifestation of the enhanced wall-normal transport by the incoming boundary layer which merges these two layers into one.

Figure 13 shows a horizontal plane of u_{rms} at $y^+ \simeq 15$, the approximate wall-normal location within the buffer layer where the maximum of the streamwise fluctuations is reached. In the laminar-inflow case, a clear signature of the shape of the horseshoe vortex can be observed, mainly due to the fact that transition to turbulence is triggered by the adverse pressure gradient from the recirculation bubble originated at the stagnation point on the obstacle. Note how the relatively less disturbed regions observed in the instantaneous field from Figure 6 are also reflected in the streamwise turbulence intensity contours, which
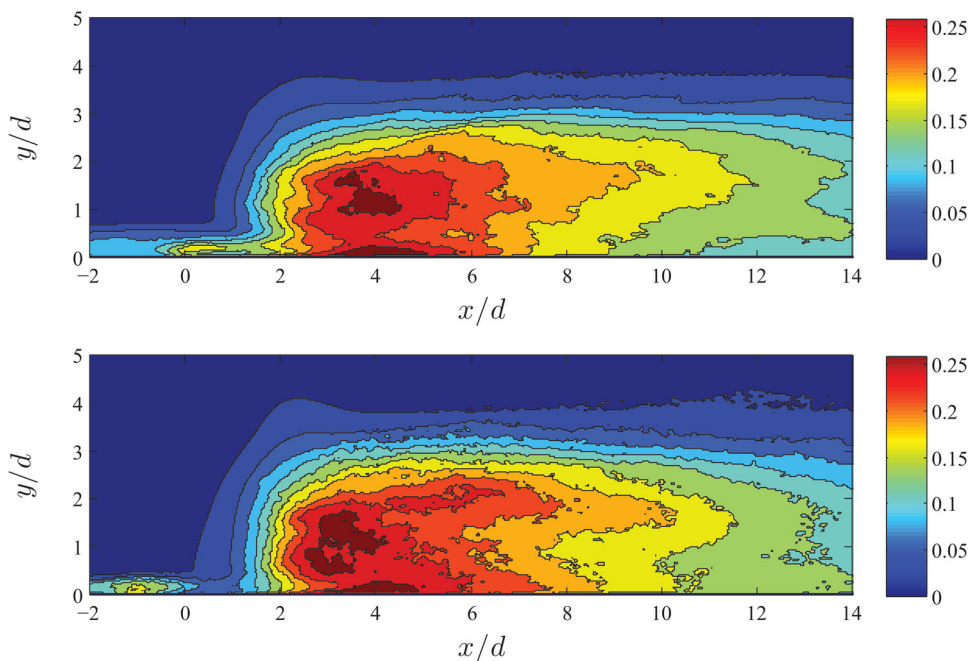
Figure 12.   Streamwise turbulent intensity fields $u_{\rm rms}$ normalized with U_∞ at a distance of $1.5d$ from the centerplane, for the (top) turbulent and (bottom) laminar-inflow simulations. Fields obtained as the average between the corresponding fields at $z = +1.5d$ and $-1.5d$.

show the transitional stage of the flow in this area. In the turbulent-inflow case, the incoming boundary layer already exhibits streamwise fluctuations with a maximum of around $u_{\rm rms,\,max} \simeq 0.1$, and at the location where it interacts with the adverse pressure gradient introduced by the geometry this value increases up to around 0.3. This is remarkable, since it is a manifestation of the fact that adverse pressure gradients force the large-scale structures of the flow, which have their footprint close to the wall (as observed experimentally by Monty et al. [44] and Harun et al. [45] at higher Reynolds numbers between $Re_\theta = 5000$ and 10,000). The regions of highly accelerated flow are also noticeable in these figures, and it is evident that these areas are wider in the laminar-inflow case. Another indicator of the attenuated turbulence intensity under the influence of the pressure gradient is shown in Figure 13 (top), where, interestingly, the values of $u_{\rm rms}$ significantly decay below 0.1, which is in agreement with the discussion above. The area of higher turbulence intensity extends farther downstream and over a wider region in the laminar-inflow case, which is an indicator of the wider wake; but it is also interesting to note that the interface between the wake region and the boundary layers on the sides is sharper in the laminar-inflow case, due to the fact that in this configuration they also exhibited turbulent fluctuations.

Additional evidence of the connection between the incoming turbulence and the horseshoe vortex is given in Figure 14, where the time-averaged wall-normal velocity fields V are shown at the planes located $1.5d$ away from the centreplane. In this figure, a strong upward motion (of around 10% the value of the freestream velocity) is observed, together with another intense downward motion, at $x/d = 0$ in the turbulent-inflow simulation. Only the descending motion is observed in the laminar case, which can be associated with the fact that in the turbulent case the near-wall turbulent cycle is clearly distorted by the effect of the
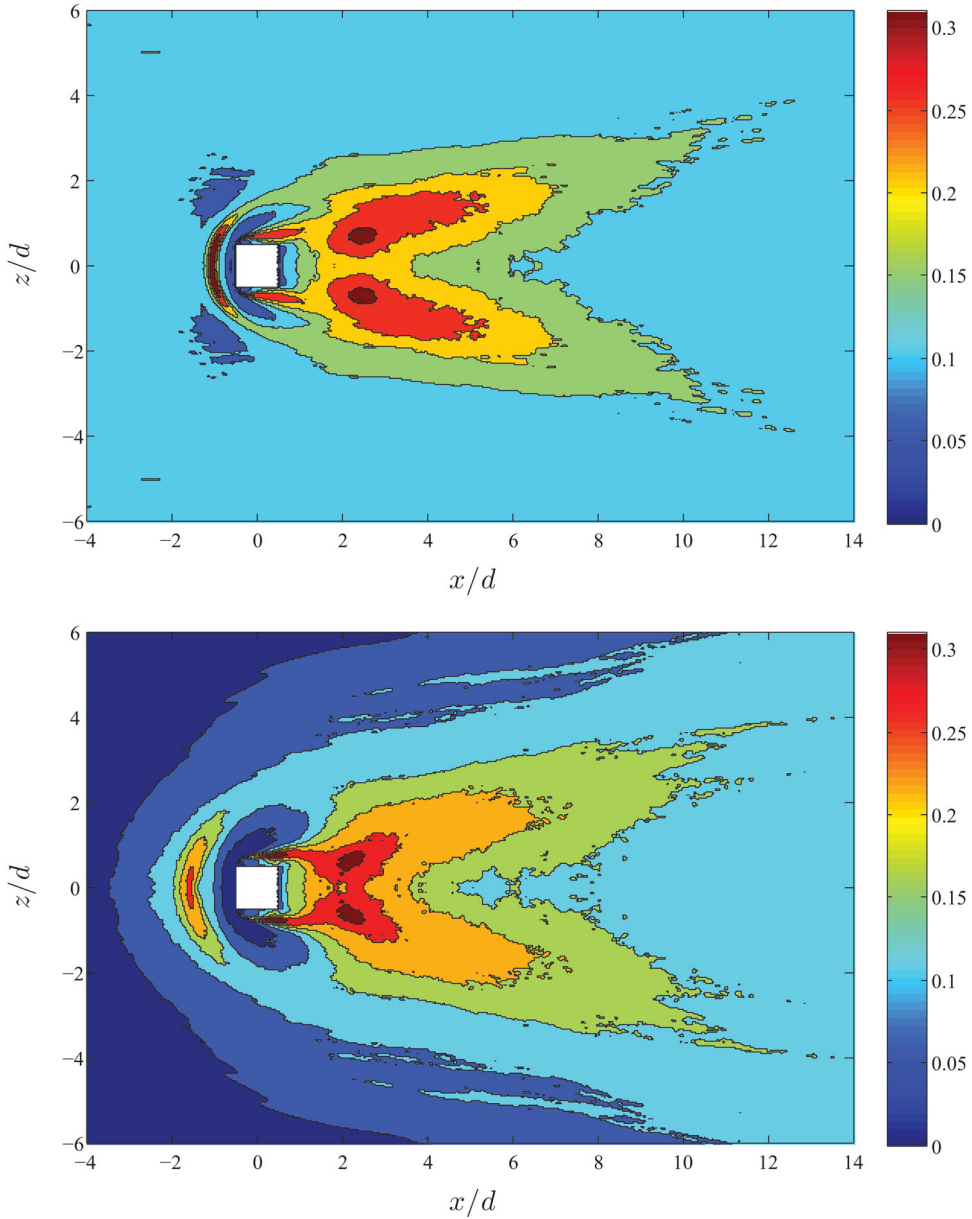
Figure 13. Streamwise turbulent intensity fields u_{rms} normalized with U_∞ at $y^+ \simeq 15$, for the (top) turbulent and (bottom) laminar-inflow simulations. Note that wall units were determined from the time-integrated turbulent-inflow profile, and this location corresponds to $y = 0.027d$.

horseshoe vortex, yielding a possible explanation of the significantly reduced turbulence intensities. Interestingly, in the laminar-inflow case a large negative value of $\overline{uv}$ (not shown) is present at this location, which indicates intense wall-normal turbulent transport. It can be conjectured that in the turbulent-inflow simulation, the adverse pressure gradient forces the turbulent structures in the incoming boundary layer, then streamwise turbulence intensity
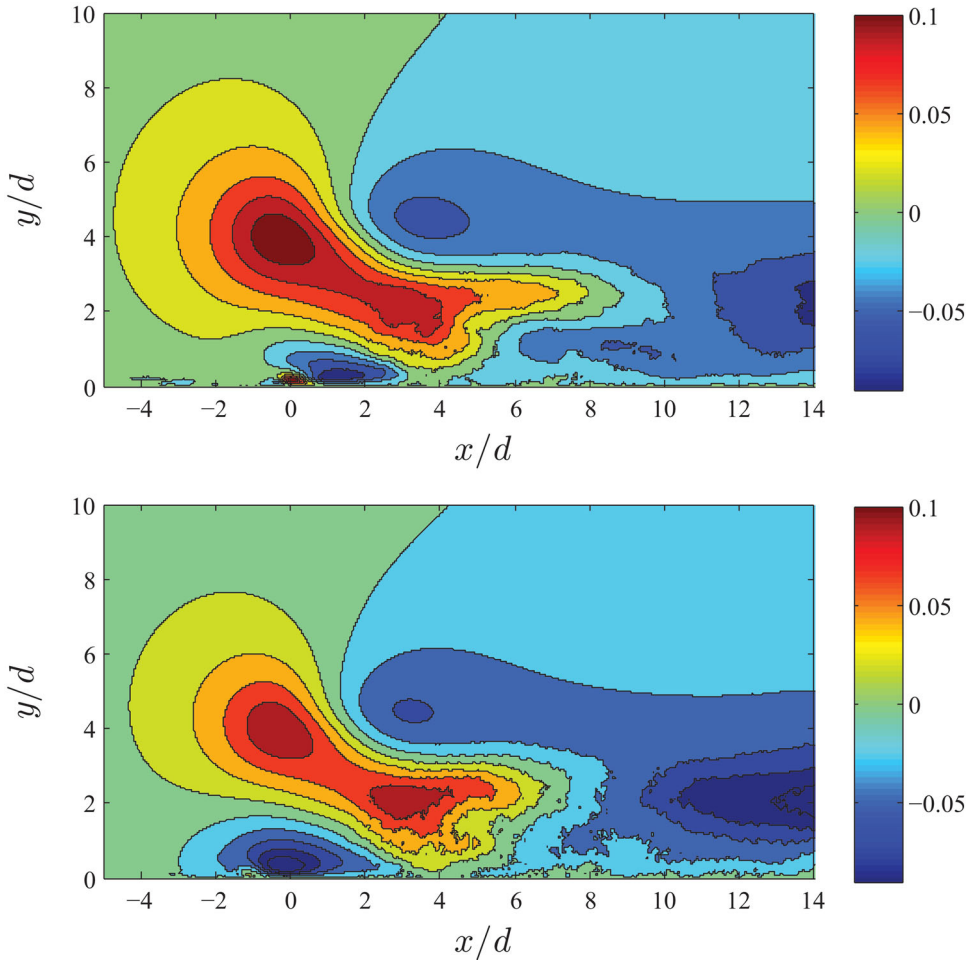
Figure 14. Time-averaged wall-normal velocity field V normalized with U_∞ at a distance of $1.5d$ from the centerplane, for the (top) turbulent and (bottom) laminar-inflow simulations. Fields obtained as the average between the corresponding fields at $z = +1.5d$ and $-1.5d$.

modulates the horseshoe vortex, feeding its streamwise vorticity. Therefore, both u_{rms} and w_{rms} are attenuated, but $\overline{uv}$ is not. In fact, the instantaneous visualisations in Figure 4 show that in the turbulent case the horseshoe vortex cannot be observed in the instantaneous realisations, which could be explained by the fact that the incoming turbulence modulates this vortex.

Figure 15 shows time-averaged streamwise velocity fields from both cases, and it becomes obvious that even if instantaneously the horseshoe vortex cannot be identified, after averaging in time it can be visualised, in agreement with Nagib and Corke.[4] It can also be observed how in the laminar-inflow simulation the boundary layer gets thicker in turbulent regions of the domain, especially past the obstacle where the influence of the horseshoe vortex is most significant.

Further understanding of the differences between the mean velocity fields can be achieved by analysing Figure 16, which shows the streamwise mean velocity U at the
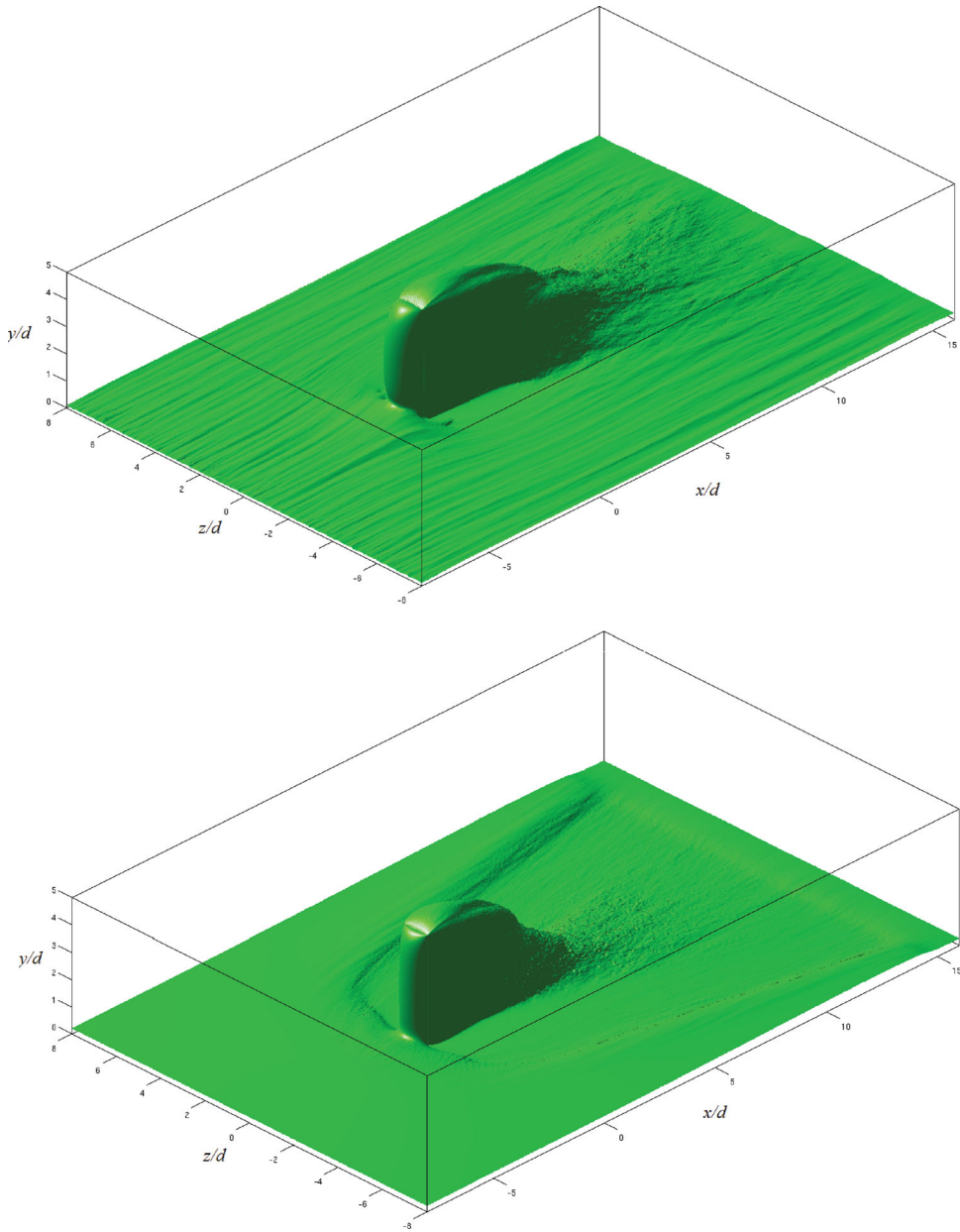
Figure 15. Time-averaged streamwise velocity fields for (top) turbulent and (bottom) laminar-inflow simulations. The panels show isosurfaces of streamwise velocity U equal to 0.7 and 0.5 times the freestream velocity U_∞ respectively, and the flow direction is from left to right. The different choice of contour levels in both cases is motivated by the fact that the horseshoe vortex is much stronger in the laminar-inflow simulation than in the turbulent-inflow case. Also note the presence of the sponge region between $x/d = 14$ and 16.
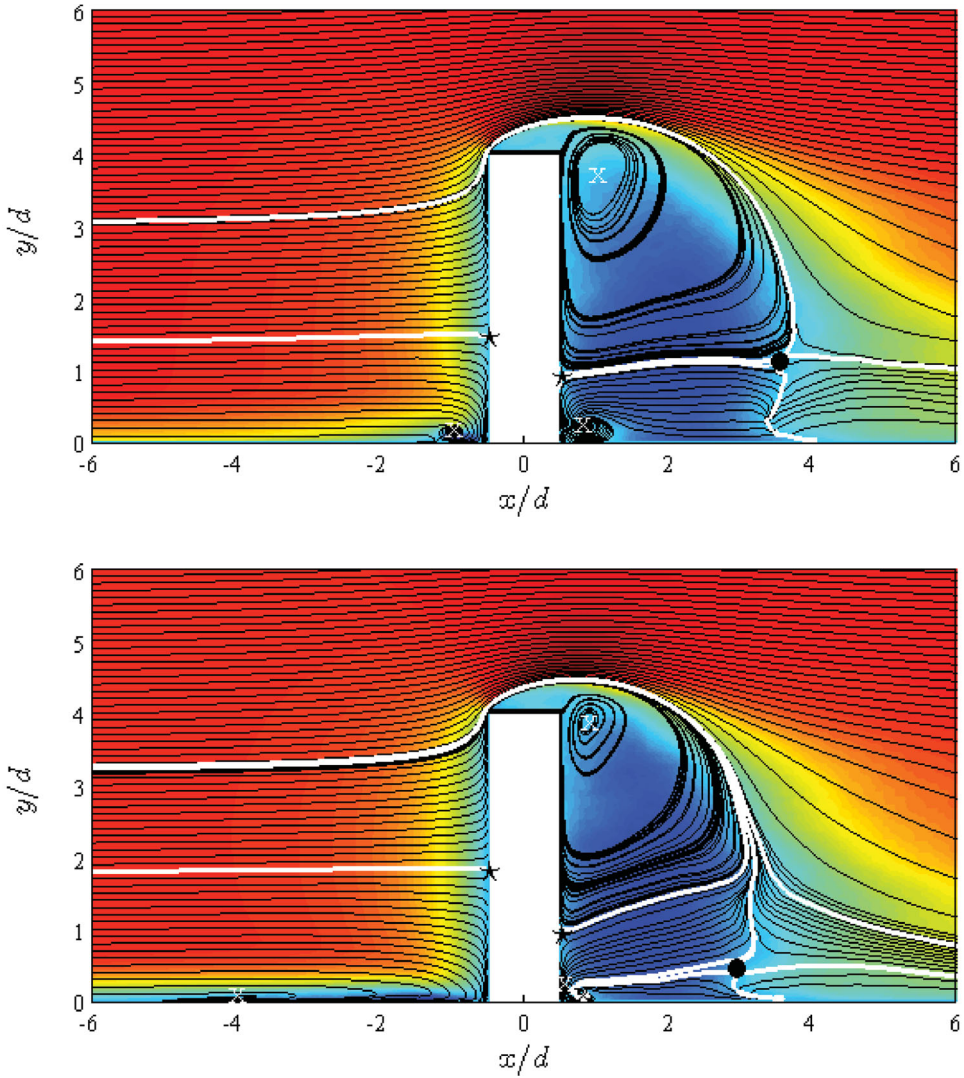
Figure 16. Time-averaged streamwise velocity U normalized with U_∞ at the centreplane of the domain $z/d = 0$ together with mean flow streamlines, for the (top) turbulent and (bottom) laminar-inflow simulations. Location of saddle points indicated by ($\bullet$), stagnation points by ($\star$) and centers of recirculating bubbles by (x).

centreplane ($z/d = 0$) for both simulations, together with the streamline pattern on that plane obtained through integration of U and V velocity components. Note that it is possible to define two-dimensional streamlines at $z/d = 0$ due to the average in time and the spanwise symmetry. Starting with both windward sides, it is interesting to observe that the stagnation point on the obstacle is at a slightly higher wall-normal location in the laminar ($y_s \simeq 1.9d$) than in the turbulent ($y_s \simeq 1.5d$) inflow case. However, in Section 2.2 we showed that the boundary layer at this location was thicker in the laminar-inflow case ($0.71d$) than in the laminar-inflow configuration ($0.64d$), which again highlights the different interactions between the adverse pressure gradient and the incoming boundary layer in both cases. This

is also manifested by the shorter recirculation bubble in the laminar-inflow case, the centre of which is located at $x \simeq -1d$, compared with a much larger recirculation bubble centred at $x \simeq -4d$ in the laminar-inflow case. This is in agreement with the streamwise turbulence intensity shown in Figure 13, and connected with the discussion regarding the modulation of the horseshoe vortex by the incoming TBL. On the other hand, the stagnation point on the leeward side is located at approximately the same height on the obstacle in both cases, $y_s \simeq 1d$, which is a manifestation of some of the similarities exhibited by both wakes very close to the cylinder. However, the structure of the wake differs for $x > 3d$, where in the turbulent case the recirculation bubble exhibits a saddle point at $x \simeq 3.5d$ and $y \simeq 1d$, and the laminar-inflow configuration shows a shorter recirculation region with a saddle point at $x \simeq 3$ and $y \simeq 0.5$. The fact that the saddle point is closer to the cylinder and to the wall in the laminar-inflow case is closely related to the $\overline{uv}$ and w_{rms} distributions at the centreplane discussed in Figures 10 and 11. Another argument supporting the similarity of the wakes close to the obstacle (which produces similar separation effects on both flows) is the fact that, although both recirculation regions differ in extension, they are centred at similar locations close to the obstacle, near $x \simeq 0.8d$ and $y \simeq 3.8d$. The very different state of turbulence in both cases causes interesting differences near the obstacle: close to the wall both flows show the centre of another recirculating region at $x \simeq 0.8d$ and $y \simeq 0.15d$, but the laminar case shows another counter-rotating vortex very close to the obstacle in the same location. This vortex impacts the upper part of the larger recirculating region, which splits into two branches at $x \simeq 3d$ and $y \simeq 2.5d$, and could be one of the agents leading to a shorter bubble in the laminar simulation. Although an onset of formation of this additional vortex may be observed in the turbulent simulation, it is not strong enough to affect the larger recirculating region in the wake. The experimental study by Wang and Zhou [27] and the LES by Chen et al. [12] at the same Reynolds number $Re_d \simeq 11,000$ show very similar streamline patterns as the one presented here in the laminar-inflow case. Chen et al. [12] also compared the effect of laminar and TBL as inflow conditions, although their laminar streamline pattern differed from the one shown in Figure 16. However, in their study the goal was to match boundary-layer thicknesses at the obstacle instead of Reynolds number as we propose here, and therefore their laminar boundary-layer simulation was performed at a much lower Re_d value of 500, which could explain this discrepancy.

3.3. *Calculation of Strouhal number*

Finally, the vortex shedding frequency is characterised by analysing the time series of streamwise velocity at $(x, y, z) = (7d, 4.2d, 3d)$. This location was chosen because the unsteadiness induced by the vortex shedding is also sensed in the freestream around the cylinder, and in this region the signal is free from turbulence and hence it is easier to evaluate. A rough estimation of the Strouhal number based on the time history of the instantaneous streamwise velocity $\tilde{u}$, where a total of 11 and 12 shedding periods are available for the turbulent and laminar-inflow cases, respectively, yields an approximate Strouhal number of $St \simeq 0.1$ in both cases. However, a better estimate of the main shedding frequency (together with the presence of other relevant, less intense frequencies in the wake) can be obtained by computing the power spectral density of this time series E_u. The sampling frequency and window size of the fast Fourier transform we used lead to an estimated frequency resolution of $\Delta f = 0.83$. Both spectra are shown in Figure 17, where again both simulations exhibit a peak around $St \simeq 0.1$, which corresponds to the main vortex shedding frequency in both wakes. It is also interesting to observe how secondary peaks around 0.2 and 0.3 (which are two orders of magnitude smaller than the main shedding) are significantly higher
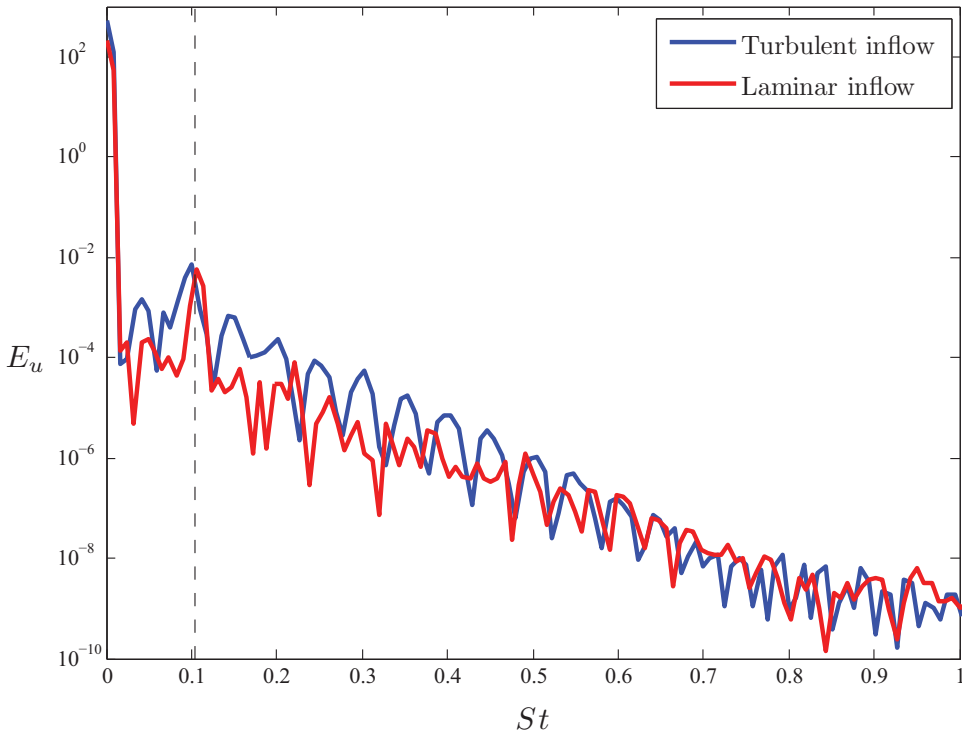
Figure 17. Power spectral density of the streamwise velocity E_u at $(x, y, z) = (7d, 4.2d, 3d)$ for both turbulent and laminar-inflow simulations.

in the turbulent case, which is connected with the more complex dynamics registered in the turbulent wake as discussed above. It is also relevant to point out that even if the two wakes exhibit different features, both have approximately the same Strouhal number, in good agreement with the experimentally measured value of $St = 0.1 \pm 0.03$ reported by Bourgeois et al. [30]. The same Strouhal number, and qualitatively similar spectra were reported by Wang and Zhou [27] in their PIV study of a wall-mounted square cylinder of height $7d$ at the same Re_d considered here. The value of 0.1 found in this study for a square cylinder of finite length is slightly lower than the one obtained in two-dimensional square cylinders, around 0.13 in this Reynolds number range, as documented by Okajima.[46] This reduced Strouhal number in the cylinder of finite length was associated with the downwash flow from the top of the obstacle by Zdravkovich [2] and by Wang and Zhou.[27] They argued that this downwash flow essentially widens the wake near the obstacle, which reduces the spanwise vortex shedding frequency, and it is in agreement with the results of this study.

3.4. *Comparison of computational results with experimental data*

After describing the main features of turbulent and laminar-inflow simulations, and high-lighting the most significant differences observed in both flows, we now compare both computations with the PIV measurements obtained by Bourgeois et al. [30] in the same geometry and nominal Reynolds number $Re_d = 11,000$. These results were used as bench-mark for comparison of the different simulations during the Challenge organised by the CFD Society of Canada in 2012. Figure 18 shows the streamwise velocity at the centreplane
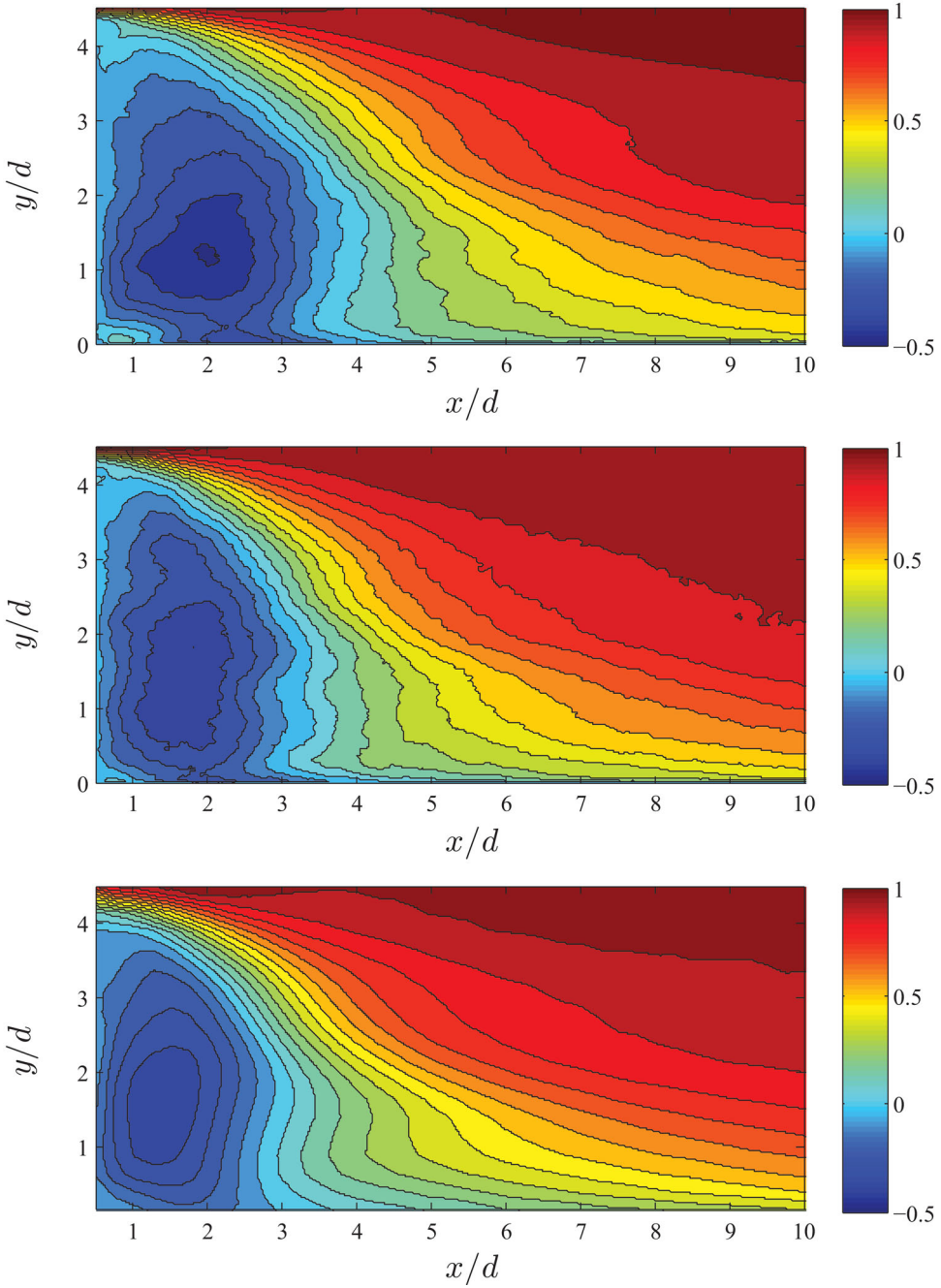
Figure 18. Time-averaged streamwise velocity U normalized with U_∞ at the centerplane ($z/d = 0$), for the (top) turbulent and (middle) laminar-inflow simulations, and the (bottom) PIV measurements by Bourgeois et al. [30].

of the domain for both simulations (averaged over a period larger than 110 convective time units, so at least 11 shedding periods) and the experimental data. All the features in the experimental wake can be observed in both simulations, and for example both simulations show the same 45° inclination in the narrowly spaced contours from around $(x, y) \simeq (2d, 4d)$ to $(x, y) \simeq (4d, 2d)$, as in the experiment. It is interesting to observe that the minimum velocity in the wake is located closer to the wall and concentrated in a smaller region in the turbulent case than in the experiment, which exhibits a more elongated region of minimum velocity in the wall-normal direction. Interestingly, the wake in the laminar-inflow simulation also exhibits the features observed in the experiment, and the narrower recirculating bubble in the wake (as discussed in Figure 16) is also in closer agreement with the experiment. Also note how the small region of positive velocity located at $x \simeq 0.5d$ close to the wall in the laminar-inflow simulation is not observed in the laminar-inflow case or the experimental results.

Figure 19 shows the mean streamwise velocity at $x = 8d$, which is further downstream than the direct area of influence of the obstacle ($x < 3d$) where both turbulent and laminar-inflow wakes exhibit very similar features. Again the main features observed in the experiment are captured by both simulations, with the exception of narrow regions of lower velocity in the freestream around $y \simeq 4d$. These could be attributed to the fact that 0.8% turbulence intensity was reported in the description of the experimental set-up, and this was not accounted for in either simulation. A more detailed comparison shows a hump in the centreplane of the wake, around $y \simeq 3.5d$, which is more pronounced in the laminar-inflow case, and smaller in both the laminar simulation and the experiment. It is also interesting to observe that the slightly wider wake in the laminar case is in better agreement with the experiment, which again shows that our laminar-inflow simulation exhibits more common features with the measurements. The mean streamwise velocity at $y \simeq 1d$ (not shown here) also reveals that the spreading rate of the laminar case is in closer agreement with the experiment than the turbulent simulation.

Finally, the streamwise turbulence intensity at a vertical plane at a distance of $1d$ above the wall is shown in Figure 20 for the three cases. The first interesting observation is the fact that despite the very different fields exhibited by the turbulent and laminar simulations close to the wall (Figure 13), farther from the wall the two flows look qualitatively similar, where the two lobes of high turbulence intensity from the two sides of the cylinder are the most relevant feature, combined with the progressive spreading with the wake. Besides, we highlight the fact that the laminar-inflow simulation exhibits a distribution quite similar to the experiment, with regions of high turbulence spanning up to $x \simeq 6d$, whereas in the turbulent case they reach $x \simeq 8d$. Nevertheless, the experiment features lower maximum values of turbulence intensity around $x \simeq 2d$, and does not show the narrow bubble of higher turbulence intensity at $x/d \simeq 1$ and $z/d \simeq 0$, which is observed in the laminar-inflow case, and could be attributed to an attenuation in the measured streamwise fluctuations.

The most relevant conclusion of this section is that, even if the three cases have the same Strouhal number, the three wakes are considerably different, especially for $x > 3d$. In other words, since separation is induced by the geometry at fixed locations, the main shedding will be relatively independent of the state of the incoming boundary layer at these Reynolds numbers, and the large-scale features of the wake right after the obstacle will be relatively similar. However, for streamwise distances larger than around $3d$ downstream of the obstacle other elements play an important role in the dynamics of the wake, such as turbulence penetrating from the sides, and its coupling with the actual wall-normal momentum redistribution. It is also important to note that the wake observed in the experiment is in better agreement with our laminar-inflow simulation than with our turbulent-inflow case, which
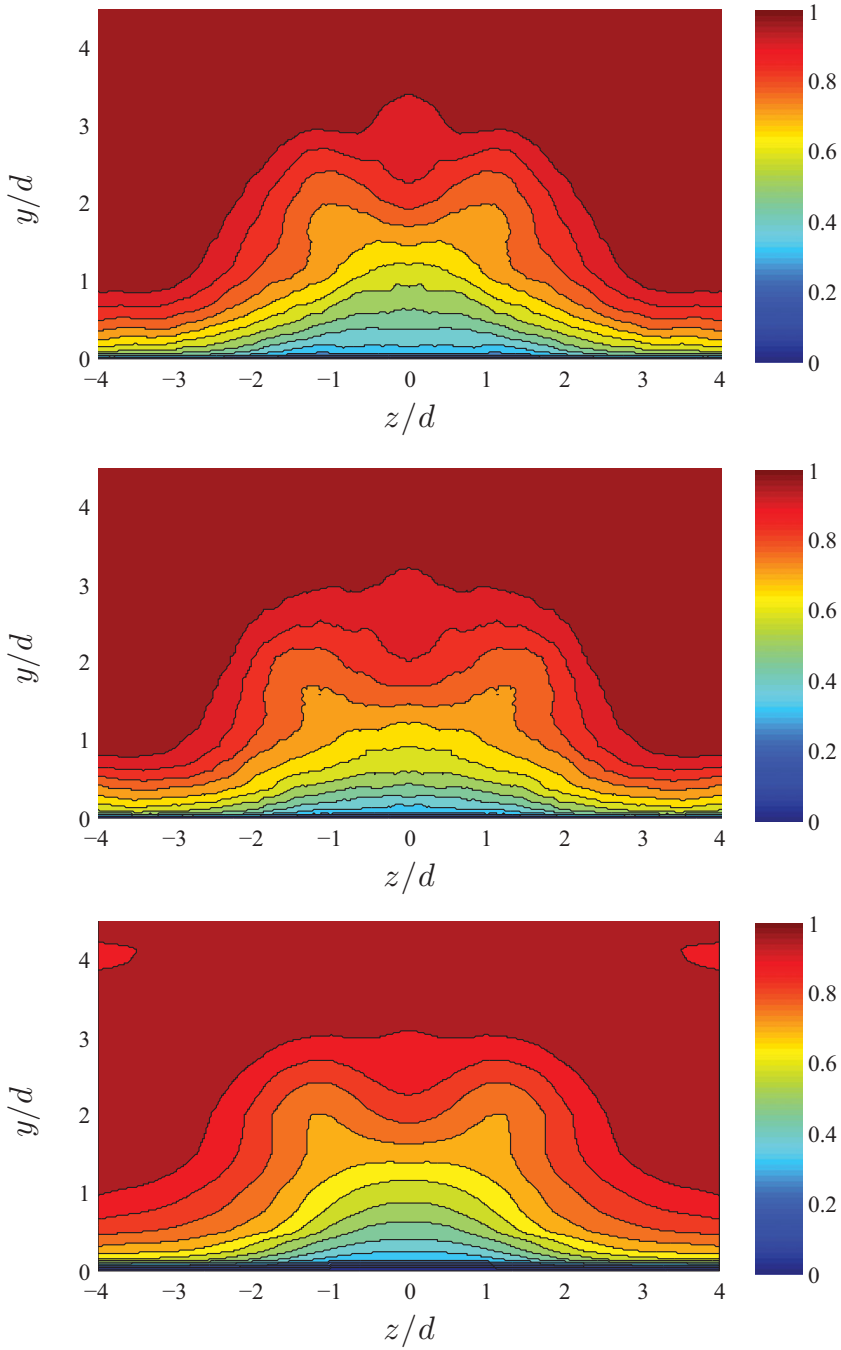
Figure 19.   Time-averaged streamwise velocity U normalized with U_∞ at $x = 8d$, for the (top) turbulent and (middle) laminar-inflow simulations, and the (bottom) PIV measurements by Bourgeois et al. [30].
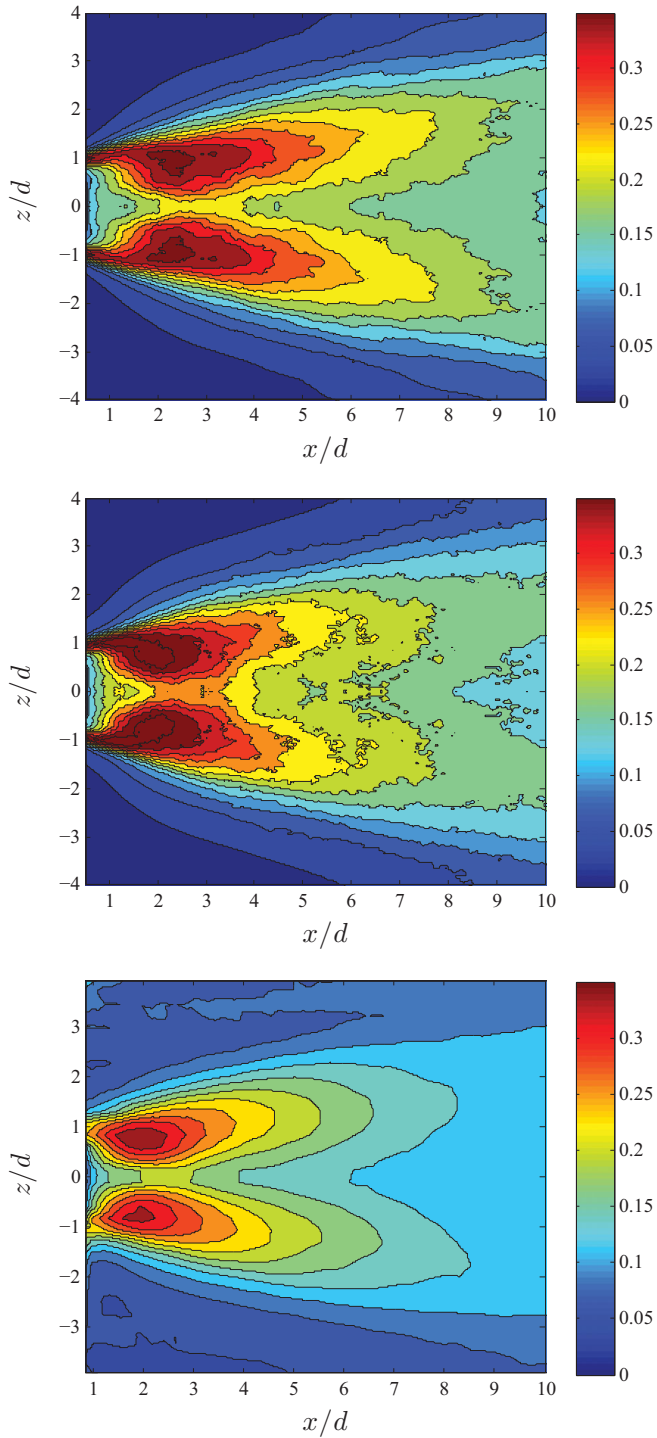
Figure 20. Time-averaged streamwise turbulence intensity u_{rms} normalized with U_∞ at $y = 1d$, for the (top) turbulent and (middle) laminar-inflow simulations, and the (bottom) PIV measurements by Bourgeois et al. [30].

indicates that the experimental tripping may have not been appropriate, and the development length insufficient. This also highlights the possibility of using DNSs to identify subtle differences in the experimental inflow conditions, which may have a significant impact on the flow field. This is particularly relevant if experimental data is used to calibrate turbulence models.

4.   Summary and conclusions

The flow around a wall-mounted square-section cylinder was investigated under two different inflow conditions by performing DNSs with the high-order spectral element code Nek5000. In the initial study, presented in the CFD Society of Canada Challenge in 2012 (Malm et al. [10]), we considered a ZPG TBL as inflow condition, which was generated by the pseudo-spectral Fourier–Chebyshev code SIMSON as a time-dependent Dirichlet condition. This approach significantly reduced the computational cost of the main simulation, aimed at solving the flow around the cylinder. Comparison of the laminar-inflow results with the benchmark data of the Challenge, consisting of PIV measurements in the same geometry (obtained by Bourgeois et al. [30]), led to an interesting conclusion: even if the computational Strouhal number of 0.1 agreed very well with the experimental value of $St = 0.1 \pm 0.03$, the two wakes exhibited noticeable differences. This motivated a second computational study, where we considered a laminar boundary layer represented by the Blasius similarity solution as inflow condition. The Blasius profile was defined such that matching Reynolds number based on momentum thickness $Re_\theta \simeq 1000$ was obtained at the obstacle ($x/d = 0$). Interestingly, the laminar boundary-layer simulation also had the same Strouhal number of 0.1, although its wake showed much closer agreement with the experimental measurements than the turbulent simulation. In light of these results, it can be conjectured that the state of the experimental boundary layer exhibits features of underdeveloped turbulence, possibly related to insufficient fetch length and/or inadequate tripping. This could very well be the case, since the experimental boundary layer is obtained by means of a sharp leading edge flat plate (as reported by Bourgeois et al. [30]), which is not as widely used as other procedures based on roughness elements.[14,47] It is also important to note that the SIMSON simulation was started a distance $28d$ upstream of the obstacle, using a volume-force tripping [48] which agrees very well with fullyturbulent experimental boundary layers, whereas in the experiment the leading edge of the plate is only $16d$ upstream of the cylinder. The impact of both tripping and development length on the state of a TBL was discussed in detail by Chauhan et al. [49]

Flow development was assessed for both simulations, and the spanwise width of the domain was found to be slightly insufficient to completely return to an unmodified flow at the planes $z/d = \pm 8$. This is especially noticeable in the laminar-inflow case, which exhibits a wider horseshoe vortex. Although this vortex can be observed even in the instantaneous fields in the laminar simulation, it is only visible in the time-averaged fields when the turbulent simulation is considered. This is in agreement with the smoke-wire visualisations by Nagib and Corke,[4] and here we find that the incoming streamwise turbulence intensity modulates the horseshoe vortex in the laminar-inflow simulation. This is also related to the fact that near-wall streaks characteristic of wall-bounded turbulence become attenuated at the accelerated regions on both sides of the cylinder. Although the favourable pressure gradient should only affect the spanwise turbulence intensity, we show evidence of the interaction between the adverse pressure gradient in front of the obstacle and the streamwise fluctuations, which significantly decay when both sides of the cylinder are investigated. The dramatic reduction of both u_{rms} and w_{rms} explain the attenuation of the streaks. It is also

interesting to highlight that both simulations have the same Strouhal number because both wakes exhibit similar features close to the obstacle ($x < 3d$), since the geometry induces similar separation processes. Further downstream the effect of the growing boundary layers on both sides of the obstacle leads to different behaviours in both wakes, where the wake associated with the laminar inflow is instantaneously wider, whereas the turbulent one is slightly wider in the time-averaged field. These differences could be further explored by performing a proper orthogonal decomposition of the flow in both wakes in a future study.

The increasingly extended use of DNSs at progressively higher Reynolds numbers and more complex geometries is now bringing the possibility of comparing experimental studies with simulations, which leads to the synergistic use of both data-sets of the same flow case. For instance, a DNS provides more detailed information of the state of the flow at any point in the domain, but experiments are faster to perform once the laboratory set-up is finalised, allowing more efficient parametric analyses which then can be used to guide the simulations. However, this study shows that when generating reference data-sets it is essential to carefully characterise all the features defining the flow, including boundary and initial conditions, so that the case under study can effectively be reproduced in other experimental and computational campaigns for adequate high-accuracy comparisons. Following the discussion in the introduction regarding the need to generate high-quality data-sets to improve currently available RANS models, the need for flow cases with properly characterised initial and boundary conditions becomes evident.

Acknowledgements

References

[1] Oertel H. Wakes behind bluff bodies. Annu Rev Fluid Mech. 1990;22:539–564.
[2] Zdravkovich MM. Flow around circular cylinders, Vol 2: Applications. New York (NY): Oxford University Press; 2003.
[3] Corke TC, Nagib HM, Tan-Atichat J. Flow near a building model in a family of surface layers. J Wind Eng Ind Aerodyn. 1979;5:139–158.
[4] Nagib HM, Corke TC. Wind microclimate around buildings: characteristics and control. J Wind Eng Ind Aerodyn. 1984;16:1–15.
[5] Monnier B, Neiswander B, Wark C. Stereoscopic particle image velocimetry measurements in an urban-type boundary layer: insight into flow regimes and incidence angle effect. Boundary-Layer Meteorol. 2010;135:243–268.
[6] Fric TF, Roshko A. Vortical structure in the wake of a transverse jet. J Fluid Mech. 1994;279:1–47.
[7] Schlatter P, Örlü R. Assessment of direct numerical simulation data of turbulent boundary layers. J Fluid Mech. 2010;659:116–126.
[8] Sillero JA, Jiménez J, Moser RD. One-point statistics for turbulent wall-bounded flows at Reynolds numbers up to $\delta^{+} \simeq 2000$. Phys Fluids. 2013;25:105102.
[9] Vinuesa R, Noorani A, Lozano-Durán A, El Khoury GK, Schlatter P, Fischer PF, Nagib HM. Aspect ratio effects in turbulent duct flows studied through direct numerical simulation. J Turbulence. 2014;15:677–706.

[10] Malm J, Schlatter P, Henningson DS, Schrader LU, Mavriplis C. Spectral element simulation of flow around a surface-mounted square-section cylinder. Proceedings of 20th Annual Conference of the CFD Society of Canada, CFD; 2012 May 9–11; Canmore, AB, Canada.

[11] Shademan M, Barron RM, Balachandar R. Analysis of vortical structures in flow over a surface-mounted square-section cylinder using large eddy simulation. Proceedings of 20th Annual Conference of the CFD Society of Canada, CFD; 2012 May 9–11; Canmore, AB, Canada.

[12] Chen Z, Hosseini Z, Martinuzzi R. The influence of boundary layer state on the wake topology of a surface mounted bluff body. Proceedings of 20th Annual Conference of the CFD Society of Canada, CFD; 2012 May 9–11, Canmore, AB, Canada.

[13] Saeedi M, LePoudre P, Wang BC. Direct numerical simulation of flow around surface-mounted square-section cylinder with AR=4. Proceedings of 20th Annual Conference of the CFD Society of Canada, CFD; 2012 May 9–11; Canmore, AB, Canada.

[14] Vinuesa R, Rozier P, Schlatter P, Nagib HM. Experiments and computations of localized pressure gradients with different history effects. AIAA J. 2014;52:368–384.

[15] Wilcox DC. Comparison of two-equation turbulence models for boundary layers with pressure gradient. AIAA J. 1993;31:1414–1421.

[16] Launder BE, Spalding DB. Lectures in mathematical models of turbulence. London: Academic Press; 1972.

[17] Menter FR. Two-equation eddy-viscosity turbulence models for engineering applications. AIAA J. 1994;32:1598–1605.

[18] Jammalamadaka A, Nagib HM. Evaluation of turbulence models for boundary layers subjected to streamwise and spanwise pressure gradients. 46th AIAA Aerospace Sciences Meeting and Exhibit 2008 Jan 7–10, Reno, Nevada. American Institute for Aeronautics and Astronautics (AIAA), Curran Associates, Inc. (Jun 2008).

[19] Uffinger T, Becker S, Delgado A. Investigations of the flow field around different wall-mounted square cylinder stump geometries. 14th International Symposium on Applications of Laser Techniques to Fluid Mechanics; 2008 Jul 7–10; Lisbon, Portugal.

[20] Launder BE. 1990. Phenomenological modeling: present... and future?,Whither Turbulence? Turbulence at the Crossroads. In: Lumley JL, editor. Proceedings of a Workshop Held at Cornell University, Ithaca, NY, 1989 Mar 2224, Lecture Notes in Physics 357. Berlin: Springer; p. 439.

[21] Luo SC, Chew YT, Ng YT. Characteristics of square cylinder wake transition flows. Phys Fluids. 2003;15:2549–2559.

[22] Luo SC, Tong XH, Khoo BC. Transition phenomena in the wake of a square cylinder. J Fluids Struct. 2007;23:227–248.

[23] Sohankar A, Norberg C, Davidson L. Simulation of three-dimensional flow around a square cylinder at moderate Reynolds numbers. Phys Fluids. 1999;11:288–306.

[24] Saha AK, Biswas G, Muralidhar K. Three-dimensional study of flow past a square cylinder at low Reynolds numbers. Int J Heat Fluid Flow. 2003;24:54–56.

[25] Williamson CHK. Three-dimensional wake transition. J Fluid Mech. 1996;328:345–407.

[26] Wang HF, Zhou Y, Chan CK, Lam KS. Effect of initial conditions on interaction between a boundary layer and a wall-mounted finite-length-cylinder wake. Phys Fluids. 2006;18:065106.

[27] Wang HF, Zhou Y. The finite-length square cylinder near wake. J Fluid Mech. 2009;638:453–490.

[28] Wang HF, Zhou Y, Mi J. Effects of aspect ratio on the drag of a wall-mounted finite-length cylinder in subcritical and critical conditions. Exp Fluids. 2012;53:423–436.

[29] Hussein HJ, Martinuzzi RJ. Energy balance for turbulent flow around a surface mounted cube placed in a channel. Phys Fluids. 1996;8:764–780.

[30] Bourgeois JA, Sattari P, Martinuzzi RJ. Coherent vortical and straining structures in the finite wall-mounted square cylinder wake. Int J Heat Fluid Flow. 2012;35:130–140.

[31] Fischer PF, Lottes JW, Kerkemeier SG. NEK5000: open source spectral element CFD solver. 2008. Available from: http://nek5000.mcs.anl.gov

[32] Patera AT. A spectral element method for fluid dynamics: laminar flow in a channel expansion. J Comput Phys. 1984;54:468–488.

[33] Maday Y, Patera AT. Spectral element methods for the Navier-Stokes equations. In Noor AK, editor. State of the art surveys in computational mechanics. New York (NY): ASME; 1989. p. 71–143.

[34] Ohlsson J, Schlatter P, Fischer PF, Henningson D. Direct numerical simulation of separated flow in a three-dimensional diffuser. J Fluid Mech. 2010;650:307–318.

[35] Malm J. Spectral-element simulations of turbulent wall-bounded flows including transition and separation. Stockholm: KTH Mechanics; 2011.

[36] Chevalier M, Schlatter P, Lundbladh A, Henningson DS. A pseudospectral solver for incompressible boundary layer flows. Tech. Rep. TRITA-MEK. Stockholm: KTH; 2007.

[37] Schlatter P, Örlü R, Li Q, Brethouwer G, Fransson JHM, Johansson AV, Alfredsson PH, Henningson DS. Turbulent boundary layers up to $Re_\theta = 2500$ studied through numerical simulation and experiments. Phys Fluids. 2009;21:051702.

[38] Lund TS, Wu X, Squires D. Generation of turbulent inflow data for spatially-developing boundary layer simulations. J Comput Phys. 1998;140:233–258.

[39] Herbst AH, Schlatter P, Henningson DS. Simulations of turbulent flow in a plane asymmetric diffuser. Flow Turbulence Combustion. 2007;79:275–306.

[40] Colonius T. Modeling artificial boundary conditions for compressible flow. Annu Rev Fluid Mech. 2004;36:315–345.

[41] Schlichting H. Boundary-layer theory. New York (NY): McGraw-Hill Series in Mechanical Engineering; 1968.

[42] Pope S. Turbulent flows. New York (NY): Cambridge University Press; 2000.

[43] Piomelli U, Balaras E, Pascarelli A. Turbulent structures in accelerating boundary layers. J Turbulence. 2000;1:1–17.

[44] Monty JP, Harun Z, Marusic I. A parametric study of adverse pressure gradient turbulent boundary layers. Int J Heat Fluid Flow. 2011;32:575–585.

[45] Harun Z, Monty JP, Mathis R, Marusic I. Pressure gradient effects on the large-scale structure of turbulent boundary layers. J Fluid Mech. 2013;715:477–498.

[46] Okajima A. Strouhal numbers of rectangular cylinders. J Fluid Mech. 1982;123:379–398.

[47] Österlund JM. Experimental studies of zero pressure-gradient turbulent boundary layer flow. Stockholm: KTH Mechanics; 1999.

[48] Schlatter P, Örlü R. Turbulent boundary layers at moderate Reynolds numbers: inflow length and tripping effects. J Fluid Mech. 2012;710:5–34.

[49] Chauhan KA, Monkewitz PA, Nagib HM. Criteria for assessing experiments in zero pressure gradient boundary layers. Fluid Dyn Res. 2009;41:021404.